1

This is a non-peer-reviewed preprint submitted to EarthArXiv.

9

A novel experimental V-Sc olivine-melt oxybarometer for arc magmas

12 Enzo-Enrico Cacciatore[a], enzo-enrico.cacciatore@unige.ch, [0009-0007-4136-6219]

13 Ivano Gennaro[a], Ivano.Gennaro@unige.ch, [0000-0002-9903-781X]

14 Kalin Kouzmanov[a], Kalin.Kouzmanov@unige.ch, [0000-0002-7327-8949]

15 Alexandra Tsay[a], Alexandra.Tsay@unige.ch

16 Zoltán Zajacz[a], Zoltan.Zajacz@unige.ch, [0000-0001-6528-7717]

17 [a]Department of Earth Sciences, University of Geneva, Rue des Maraichers 13, 1205 Geneva,
18 Switzerland

19

20 # A novel experimental V-Sc olivine-melt oxybarometer for arc

21 # magmas

22 Enzo-Enrico Cacciatore[a], Ivano Gennaro[a], Kalin Kouzmanov[a], Alexandra Tsay[a], and Zoltán

23 Zajacz[a]

24 [a]Department of Earth Sciences, University of Geneva, Rue des Maraichers 13, 1205 Geneva,

25 Switzerland

26 Corresponding author: Enzo-Enrico Cacciatore, enzo-enrico.cacciatore@unige.ch

27

28 ## Abstract

29 Redox conditions significantly affect phase equilibria, the availability and mobility of

30 heterovalent elements, including volatiles (i.e., S) and metals (e.g., Fe, Cu) in silicate melts.

31 Gaining a deeper understanding of the initial redox state of magmas may help better

32 understand magmatic ore fertility, volcanic degassing, and the redox evolution of Earth's

33 crust and atmosphere.

34 This study reports an optimized V and novel V-Sc olivine-melt oxybarometers,

35 developed using existing V-partitioning data and new results from a series of fractional

36 crystallization experiments. Experiments were conducted in a rapid-quench molybdenum-

37 hafnium carbide pressure vessel apparatus equipped with a custom-designed hydrogen

38 membrane for flexible, precise, and accurate oxygen fugacity (fO$_2$) control. They were

39 performed at constant pressure (P = 200 MPa) and variable temperatures (T = 1019-

40 870 °C), under water-saturated conditions at fO$_2$ ranging from -1 to +3.5 log units relative to

41 the FMQ buffer. The impact of the system's composition (X) was evaluated by comparing

42 two distinct liquid lines of descent (medium-K-calk-alkaline and shoshonitic) through

43 simultaneous experiments using two capsules in parallel. The results show that the partition

44 coefficient of V between olivine and melt $(D_V^{[Ol/melt]})$ is not systematically affected by varying

45 *P-T-X* and highly correlates with changing fO$_2$, thus suggesting that the minor variations

46 observed on a global $f\mathrm{O}_2$ scale rather reflect analytical and experimental uncertainties. The

47 updated empirical calibrations allow the determination of log$f\mathrm{O}_2$ as ΔFMQ from measured

48 1) $\mathrm{D}_{\mathrm{V}}^{[\mathrm{Ol/melt}]}$ and 2) $\mathrm{K}_{\mathrm{D[V/Sc]}}^{[\mathrm{Ol/melt}]}$, expressed by the following equations:

49 $$1)\ \Delta FMQ = -1.72333\ \pm\ 0.0473 - \left(\frac{\log_{10}[(1.2273 - \log(\mathrm{D}_{\mathrm{V}}^{[\mathrm{Ol/melt}]}))\ /\ (\log(\mathrm{D}_{\mathrm{V}}^{[\mathrm{Ol/melt}]}) + 3.11912\ )]}{-0.09895\ \pm\ 0.00175} \right)$$

50 for NBO/T (non-bridging oxygens per tetrahedrally coordinated cation) ≤ 0.6:

51 $$2)\ \Delta FMQ = (\log(K_{D[V/Sc]}^{[Ol/melt]}) + 0.98079 \pm 0.02244)\ /\ {-0.20567} \pm 0.01231$$

52 In the log$f\mathrm{O}_2$ range of FMQ -1 to FMQ +3.5, relevant for arc magmatism, and at

53 hydrous conditions, both oxybarometers show 2σ calibration uncertainty below 0.5 log units.

54 The updated and new V-based oxybarometers enhance robustness across a wide *P-T-X-f*O_2

55 range, enabling accurate quantification of the redox state of magmatic systems. They can,

56 in turn, be applied to volcanic rocks ranging from basaltic to andesitic compositions by using

57 suitable olivine-hosted silicate melt inclusions to reconstruct the redox history of deep-

58 seated magma reservoirs in subduction zones. In addition, we demonstrate that the olivine–

59 melt $\mathrm{Fe_T}$-Mg exchange coefficient (where $\mathrm{Fe_T}$ is total iron expressed as FeO) correlates with

60 changing $f\mathrm{O}_2$ and can serve as an Fe-Mg oxybarometer within the calibrated range of this

61 study. Owing to the rapid diffusion of Fe in olivine, this approach can record rapid redox

62 fluctuations and provides complementary constraints to the more robust V-based

63 oxybarometers.

64 Keywords: experimental oxybarometers, olivine-melt equilibrium, V-Sc partitioning,

65 fractional crystallization, hydrous arc magmas

66

1. Introduction

68 The redox state of magmas affects the genesis of magmatic-hydrothermal ore

69 deposits (Zajacz et al., 2011, 2012; Park et al., 2021; Farsang and Zajacz, 2025), volcanic

70 degassing (Burgisser and Scaillet, 2007; Park et al., 2021; Métrich, 2022; Moretti and

71 Neuville, 2022; Ai et al., 2024; Farsang and Zajacz, 2025), and igneous phase equilibria in

72 general. Oxygen fugacity (fO_2) is the principal thermodynamic variable used as a measure

73 of the redox state of magmas. Its value is commonly expressed in reference to buffer

74 assemblages such as fayalite-magnetite-quartz (FMQ) as logfO_2 = FMQ ±x, where x equals

75 a relative value below or above FMQ (Eugster, 1957; Ballhaus et al., 1991; Cicconi et al.,

76 2020). In this study we use the definition for the FMQ buffer as outlined in Ballhaus et al.

77 (1991). By controlling the oxidation state of heterovalent elements (i.e., Fe^{2+} vs. Fe^{3+}), fO_2

78 governs phase equilibria, polymerization of silicate melts and element partitioning between

79 mineral, melts and fluids. Besides pressure (P) and temperature (T), it is a key driver of the

80 geochemical differentiation of Earth's interior (Muan and Osborn, 1956; Carmichael, 1991;

81 Frost, 1991; Kress and Carmichael, 1991; Brounce et al., 2015; Arató and Audétat, 2017;

82 Moretti and Neuville, 2022). Regarding magma differentiation, fO_2 influences the direction of

83 liquid lines of descent (LLD) and thus affects the physicochemical properties of a magmatic

84 system (Frost, 1991; Mallmann and O'Neill, 2013; Arató and Audétat, 2017; Bucholz and

85 Kelemen, 2019; Wang et al., 2019; Tassara et al., 2020; Cottrell et al., 2021; Marxer et al.,

86 2021).

87   Magmatism at convergent plate margins is characterized by elevated fO_2 compared to

88 their counterparts in other geodynamic settings (Aeolous Lee et al., 2005; Evans, 2012;

89 Cottrell et al., 2021; Zhao et al., 2022). This characteristic may play an important role in the

90 development of calc-alkaline differentiation trends and also leads to the fertility of magmatic

91 hydrothermal Cu-Au-Mo ore systems (Lee et al., 2012; Chiaradia, 2014; Park et al., 2021;

92 Ai et al., 2024). Despite its significance, the origin of magma oxidation in arc settings is still

93 debated. It has been proposed to develop either due to the flux of oxidizing slab fluids into

94 the mantle wedge (Evans, 2012; Kelley and Cottrell, 2012; Brounce et al., 2015; Cottrell et

95 al., 2021) or during magma differentiation in response to the crystallization of Fe^{2+}-rich

96 minerals or volatile loss (Sato, 1978; Aeolous Lee et al., 2005; Lee et al., 2010; Tang et al.,

97 2018). Consequently, oxybarometers that can be applied to hydrous magmas over a broad

98 P-T-compositional (X) range and that are resistant to low-temperature re-equilibration are

99 essential for gaining a deeper understanding of the above processes (Osborn, 1959;

100 Ballhaus et al., 1991; Frost, 1991; Blundy et al., 2020; Cicconi et al., 2020; Moretti and

101 Ottonello, 2022). One such method is based on Vanadium (V) partitioning between mafic

102 minerals and silicate melt. Vanadium is a heterovalent element with multiple stable oxidation

103 states (V^{2+}, V^{3+}, V^{4+}, and V^{5+}). It becomes increasingly incompatible in olivine with increasing

104 fO_2, thus allowing the olivine/melt bulk partition coefficient of V ($D_V^{[Ol/melt]}$) to be used as an

105 oxybarometer (Canil, 1997; Mallmann and O'Neill, 2013; Mallmann et al., 2022). According

106 to Shishkina et al. (2018), V has low diffusivity making it more robust against post magmatic

107 changes than other redox-sensitive elements (i.e., Fe). Numerous experimental studies have

108 been published assessing the oxybarometric potential of V leading to the development of

109 various empirical calibrations based on new input within the *P-T-X-fO$_2$* parameter space (i.e.,

110 Canil, 1997; Shearer et al., 2006; Mallmann and O'Neill, 2013; Leuthold et al., 2023).

111 However, only a few studies have calibrated the V-in-olivine oxybarometer at elevated

112 pressure in the presence of hydrous melts, conditions typical of magma differentiation at

113 convergent plate boundaries (Mallmann and O'Neill, 2009; Shishkina et al., 2018; Wang et

114 al., 2019; Erdmann et al., 2024). The present study extends the existing dataset to lower

115 temperature (*T* < 1030 °C) at high pressure (*P* = 200 MPa) and water-saturated conditions.

116 Furthermore, the effect of melt composition was also tested by using medium-K-calk-alkaline

117 (MKCA) and shoshonitic (SHOSH) starting compositions, bracketing the typical range of

118 magma compositions at convergent plate margins. A prototype externally heated cold-seal

119 pressure vessel apparatus equipped with a custom-designed hydrogen membrane was used

120 to run the experiments, which facilitated both flexible, precise and accurate fO_2 control as

121 well as rapid quenching (Alex and Zajacz, 2022; Farsang and Zajacz, 2025).The experiments

122 follow a temperature-controlled fractional crystallization series with systematically varied

123 fO_2, directly addressing the call of Marxer et al. (2021), who emphasized the key role of

124 redox conditions in arc magma differentiation.

125   In turn, by combining the new data with preexisting experimental data using statistical

126 analysis, we enhance the robustness and accuracy of V-in-olivine oxybarometry for hydrous

127 arc magmatic systems. Furthermore, we examine the Fe-Mg exchange coefficient between

128 olivine and silicate melt as an additional tool for tracking redox conditions.

2. Experimental methods

2.1. Experimental strategy

To test the potential influence of silicate melt composition, two distinct hydrous basaltic compositions were used as initial starting material to represent typical MKCA and SHOSH magmatic series encountered in subduction zone settings based on literature data from the EarthChem database (Earthchem Portal, 2021). All experiments were conducted at P = 200 MPa and water-saturated conditions. The glass matrix of the run products constrained the starting material composition for the subsequent experiment within the same fractional crystallization series. This facilitated the tracing of individual LLDs while avoiding a high degree of crystallization. Fractional crystallization series experiments were conducted with both starting materials at 5 different fO$_2$ between FMQ-1 and FMQ+3.5 with a step size of about 1 log unit encompassing much of the range of Earth's magmatism. The temperature steps for each series were the following: 1030, 990, 960, 920, and 870 °C.

2.2. Starting material

As in fractional crystallization series experiments, a new starting composition is used at each temperature and fO$_2$ step, the use of a powdered synthetic starting material is preferred over the use of a starting glass (Nandedkar, 2014; Marxer et al., 2021). To prepare these, high-purity commercial oxide and silicate powders were utilized, except for sodium (Na) and potassium (K). The latter were added in the form of in-house-prepared K- and Na-rich aluminosilicate glasses (see Table S.1 in the supplementary material). A mixture of metallic Fe and Fe$_2$O$_3$ was used in proportion calculated for each experiment using the method of Kress and Carmichael (1991) to match the expected Fe^{2+}/Fe^{3+} ratio in the silicate melt at the target fO$_2$. In-house made trace element doped peralkaline aluminosilicate glass was used to introduce trace elements (5.4 wt.%, c.f. Table S.1). Their concentrations in the starting material was chosen similar to Nandedkar et al. (2014) to ensure that Henry`s law was not violated. All components were thoroughly homogenized in an agate mortar under ethanol. The solid starting materials were then dehydrated and stored in a vacuum desiccator. Compositions of the starting materials are summarized in Table 1.

157   Table 1. Major element composition (wt.%) of the starting materials.

N o.	[a]Experi- ment	SiO$_2$	TiO$_2$	Al$_2$O$_3$	FeO -tot	MnO	MgO	CaO	P$_2$O$_5$	Na$_2$O	K$_2$O	Total -dry	[b]FeO/ Fe$_2$O$_3$
1	E7.0_II_ SB_A	50.6	0.9	16.0	8.9	0.2	9.6	10.2	0.2	2.6	0.7	100	0.43
2	E7.0_II_ SB_B	51.1	1.1	14.4	8.4	0.2	9.0	9.0	0.7	2.7	3.4	100	0.44
3	E1.1_IV _H2_A	55.9	1.1	19.5	5.0	0.1	4.8	8.7	0.3	3.7	0.9	100	0.25
4	E1.1_IV _H2_B	55.4	1.1	19.2	4.7	0.2	4.1	7.2	1.1	3.8	3.3	100	0.23
5	E3.1_II_ SB_A	55.9	1.1	18.8	5.5	0.2	4.9	8.8	0.4	3.5	0.9	100	0.28
6	E3.1_II_ SB_B	55.4	1.0	18.8	4.9	0.2	4.1	7.4	1.0	3.9	3.3	100	0.27
7	E4.1_IV _H2_A	51.9	1.0	17.8	8.7	0.1	6.4	10.4	0.2	2.7	0.7	100	0.36
8	E4.1_III _H2_B	53.1	1.2	16.0	8.1	0.1	5.6	9.5	0.8	2.8	2.8	100	0.35
9	E4.1_IV _H2_B	53.1	1.2	16.0	8.1	0.1	5.6	9.5	0.8	2.8	2.8	100	0.35
10	E2.1_III _H2_A	51.8	1.0	18.5	8.0	0.2	5.8	10.5	0.3	3.1	0.8	100	0.39
11	E2.1_III _H2_B	52.9	1.3	16.9	7.8	0.2	4.8	8.6	0.9	3.4	3.3	100	0.38
12	E7.1_S B_II_A	53.3	1.2	19.3	6.7	0.2	4.8	10.0	0.3	3.2	0.9	100	0.44
13	E7.1_S B_II_B	53.5	1.3	18.2	6.6	0.3	4.1	8.3	0.9	3.4	3.4	100	0.44
14	E1.2_H 2_A	59.8	1.3	19.1	3.8	0.2	3.6	6.6	0.5	4.1	1.1	100	0.26
15	E1.2_H 2_B	57.3	1.1	20.5	3.4	0.2	3.6	6.6	0.9	3.9	2.5	100	0.28
16	E3.2_S B_A	57.4	1.2	18.9	5.3	0.2	4.2	7.8	0.4	3.8	0.8	100	0.29
17	E3.2_II_ H2_A	57.4	1.2	18.9	5.3	0.2	4.2	7.8	0.4	3.8	0.8	100	0.29
18	E3.2_S B_B	56.2	1.0	19.4	4.9	0.2	3.8	6.9	1.1	3.9	2.6	100	0.29
19	E3.2_II_ H2_B	56.2	1.0	19.4	4.9	0.2	3.8	6.9	1.1	3.9	2.6	100	0.29
20	E3.2_IV _H2_B	56.2	1.0	19.4	4.9	0.2	3.8	6.9	1.1	3.9	2.6	100	0.29
21	E5.2_H 2_A	54.9	1.1	19.5	6.1	0.2	5.3	8.4	0.4	3.5	0.7	100	0.31
22	E4.2_II_ H2_A	53.6	1.0	19.4	7.1	0.2	5.1	9.6	0.3	3.0	0.7	100	0.37
23	E4.2_H 2_B	54.9	1.2	18.1	6.4	0.2	4.4	7.9	0.9	3.1	2.8	100	0.36
24	E4.2_II_ H2_B	54.9	1.2	18.1	6.4	0.2	4.4	7.9	0.9	3.1	2.8	100	0.36
25	E2.2_III _H2_A	53.0	1.1	19.5	7.5	0.2	4.7	9.2	0.4	3.6	0.8	100	0.38
26	E2.2_III _H2_B	53.7	1.5	18.5	7.0	0.2	4.0	8.0	1.0	3.5	2.7	100	0.40
27	E7.2_II_ SB_A	55.5	1.5	19.1	5.9	0.2	4.2	8.6	0.4	3.5	0.9	100	0.45
28	E7.2_II_ SB_B	55.6	1.5	18.4	5.5	0.3	3.8	7.5	1.0	3.3	3.2	100	0.43
29	E4.3_H 2_A	56.4	1.1	19.6	6.6	0.2	3.6	7.1	0.5	3.8	1.1	100	0.35

158

159　Table 1. (continued).

N o.	[a]Experi- ment	SiO$_2$	TiO$_2$	Al$_2$O$_3$	FeO -tot	MnO	MgO	CaO	P$_2$O$_5$	Na$_2$O	K$_2$O	Total -dry	[b]FeO/ Fe$_2$O$_3$
30	E2.3_II_ H2_A	55.6	1.2	18.8	7.2	0.2	4.1	8.2	0.5	3.5	0.8	100	0.41
31	E2.3_II_ H2_B	54.8	1.6	18.7	6.5	0.1	3.9	7.5	1.0	3.3	2.7	100	0.39
32	E7.3_S B_A	58.7	1.7	18.4	5.4	0.2	3.3	6.7	0.6	4.0	1.1	100	0.46

160　[a]Experiments ordered by decreasing temperature: .0, .1, .2, and .3 being equivalent to 1019,
161　990, 960, and 920 °C, respectively. fO_2 control is either through SB (solid buffer) or H2
162　(hydrogen membrane). A and B denote medium-K-calk-alkaline (MKCA) and shoshonitic
163　(SHOSH) starting material, respectively. In the labeling system (e.g., E7.0_II_SB_A), the
164　Roman numeral indicates the n-th experimental attempt.

165　[b]Calculated FeO/Fe$_2$O$_3$ ratio based on added Fe$_2$O$_3$- and metallic Fe-powder.

2.3. Capsule preparation

167　　　Pure Au capsules were used for experiments conducted at temperature below

168　1000 °C, while an Au$_{92.5}$Pd$_{7.5}$ (by wt.%) alloy was employed for temperature exceeding

169　1000 °C. Each experimental iteration consisted of two capsules (OD: 3 mm, ID: 2.8 mm,

170　length:10 mm). These were loaded with dry synthetic starting powders (~20 mg) of either

171　MKCA (labeled as "A" in Table 1) or SHOSH ("B") composition and 2 mg of distilled water

172　to ensure water saturation. The capsules were welded shut using a Lampert Puk V5

173　professional welder. They were tested afterwards for potential leaks by exposing them to

174　120 °C for 30 min and only capsules without weight loss were used for the experiments. To

175　maintain the proximity between the two inner capsules, a larger holder capsule (5 mm OD,

176　4.7 mm ID, length: 12-20 mm) was employed, with one end sealed. Potential Fe loss was

177　monitored using mass balance calculations, revealing only minor loss, with a maximum of

178　less than 13 rel.%. observed in the most reducing experiments (FMQ -1, Table 3). A Co-CoO

179　solid buffer (CCO) was employed for experiments conducted under reducing conditions at

180　FMQ -1 due to technical limitations associated with the hydrogen buffer technique. For the

181　secondary quality assessment of redox control, a more oxidizing solid buffer (Re-ReO$_2$) was

182　utilized to constrain fO_2 to FMQ +2.5. In both instances of applying solid buffers, a double

183　capsule technique was implemented, where the solid buffer powder was contained within a

184　partially open Pt capsule (4 mm OD, 3.7 mm ID, length: 11 mm) positioned behind the

185 experimental capsules. Subsequently, all three inner capsules were enveloped within an

186 outer Au capsule (5 mm OD, 4.4 mm ID, length: ~27.5 mm**)**, and adequate distilled water

187 was added to preserve buffering capacities before sealing (for capsule design see

188 supplementary Figure S.1). In the following sections, we distinguish experimental runs with

189 fO_2 control achieved by solid buffer (SB) from those where a hydrogen membrane (H_2) was

190 applied.

2.4. Experimental apparatus

192 Experiments were conducted in an externally heated cold-seal molybdenum-hafnium

193 carbide (MHC) pressure vessel apparatus at the Mineral Resources and Geofluids Research

194 Laboratory at the University of Geneva. Argon gas was used as a pressure medium

195 monitored with an accuracy of < 20 bars by using a digital pressure transducer calibrated

196 against a certified Ashcroft (Heise) analog gauge. An MHC vessel equipped with a single

197 cold-seal extension was employed for SB runs. When using a CCO buffer, hydrogen

198 (PH_2 = 10-13 bars at room temperature) was added to the argon pressure medium to extend

199 the lifetime of the buffer (Alex and Zajacz, 2020). For H_2 runs, an MHC vessel was coupled

200 with a semi-permeable hydrogen membrane (Shaw membrane), allowing flexible in-situ

201 control of PH_2 while maintaining fast quench capabilities (Alex and Zajacz, 2022). The first

202 set of experiments at 1030 °C was conducted under constant but higher than intended fO_2

203 conditions due to unrecognized reduced performance of the hydrogen membrane and

204 therefore excluded for the fO_2 calibration of trace element-based olivine oxybarometry

205 except for the CCO-runs (for run conditions of all experiments, see Table S.2).

206 Temperature control was ensured via K-type thermocouple with an accuracy of ±3 °C.

207 The temperature inside the vessel was calibrated semi-annually against the external

208 thermocouple by using internal thermocouples at P = 200 and 100 MPa (no significant

209 pressure effect observed). The temperature gradient within the hot zone was also estimated

210 by using internal thermocouples of varying length. For both H_2- and SB-runs the temperature

211 gradient along the capsules' length was below 10 °C. In the case of the applied double-

212 capsule technique in SB-runs, the target temperature was adjusted to the capsule's center

213 at 15 mm below the hot end, where the difference between the capsule's center and the cold

214   end was about 10 °C. Once thermal stability was reached during SB runs, the capsules were

215   dropped into the hot zone. The standard run procedure for H_2-runs was as follows: A

216   bracketing approach was chosen to estimate the PH_2 within the vessel under run conditions

217   and adjusted to the desired PH_2 if needed (Farsang and Zajacz, 2025). Note that on our

218   apparatus, the Shaw membrane can be turned from supply to monitoring function by the

219   closure of a single valve. All experiments began once steady-state equilibrium between

220   external and internal PH_2 was established, at which point the capsule was dropped into the

221   hot zone. The PH_2 was monitored using a factory-calibrated digital pressure-transducer with

222   ±0.25% full-scale error (Alex and Zajacz, 2020). Depending on the target PH_2, three pressure

223   transducers were used for the best precision and accuracy with the following ranges: I) 0–

224   68.95 ±0.17 bar, II) 0–34.47 ±0.09 bar, and III) 0-2.068 ±0.005 bar. At a given fH_2, fO_2 inside

225   the capsule was imposed by the water breakdown reaction ($2H_2+O_2 \leftrightarrow 2H_2O$) (Gorman and

226   Nardella, 1962; Shaw, 1963; Hewitt, 1977; Gunter et al., 1979; Scaillet et al., 1992). The

227   value of fH_2O at run conditions was calculated by using the equation of states of Churakov

228   and Gottschalk (2003). The run fO_2 was recalculated considering the temperature gradient

229   and fluctuations in applied pressure and PH_2 to obtain an uncertainty of the imposed fO_2.

230   For some experimental SB-runs, temperature cycling with ±10 °C amplitude for around total

231   16 h was applied to enhance crystal growth similar to da Silva et al. (2017). Temperature

232   oscillation was applied at the beginning of the experiment and completed in 6 cycles. High

233   and low set temperatures were reached within 5 and 30 min, respectively, and then held

234   constant for 1 h each to ensure thermal equilibrium. In experiment E5_2_A an amplitude of

235   ±15 °C was applied. All experimental parameters are summarized in Table 2.

236

237   Table 2 Summary of run conditions.

Run	[a]SM	t (h)	[b]fH$_2$ (bar)	[c]$\pm\Delta$ fH$_2$ (bar)	log$f$O$_2$ (bar)	[d]$\pm\Delta$ log$f$O$_2$ (bar)	log$f$O$_2$ (ΔFMQ)	[d]$\pm\Delta$ log$f$O$_2$ (ΔFMQ)	P (bar)	[e]$\pm\Delta$ P (bar)	T (°C)	[f]$\pm\Delta$ T (bar)	T_{cyc} (°C)
E7_0_II-SB	A and B	18	nd	nd	-11.54	0.15	-0.87	0.15	2011	13	1019	10	nd
E1_1_IV-H2	A and B	60	0.46	0.17	-7.55	0.41	3.56	0.41	2004	67	990	10	nd
E3_1_II-SB	A and B	49	nd	nd	-8.57	0.14	2.54	0.15	1975	85	990	10	nd
E4_1_III-H2	B	59	7.06	0.07	-9.92	0.01	1.19	0.05	2016	13	990	10	nd
E4_1_IV-H2	A and B	60	7.41	0.32	-9.96	0.04	1.15	0.06	2020	38	990	10	nd
E2_1_III-H2	A and B	62	19.46	1.45	-10.80	0.07	0.31	0.08	2013	5	990	10	nd
E7_1_II-SB	A and B	48	nd	nd	-11.97	0.15	-0.86	0.16	1983	27	990	10	10
E1_2-H2	A and B	72	0.55	0.04	-8.22	0.06	3.37	0.08	2019	12	960	10	nd
E3_2-SB	A and B	56	nd	nd	-9.01	0.15	2.58	0.16	2044	12	960	10	10
E3_2_II-H2	A and B	28	1.88	0.08	-9.29	0.04	2.30	0.06	2007	55	960	10	nd
E3_2_IV-H2	B	106	1.86	0.02	-9.28	0.01	2.31	0.05	2018	15	960	10	nd
E5_2-H2	A	117	3.05	0.04	-9.32	0.38	2.27	0.39	2044	40	960	15	15
E4_2-H2	B	72	8.63	0.49	-10.61	0.05	0.97	0.07	2020	11	960	10	nd
E4_2_II-H2	A and B	72	8.20	0.40	-10.57	0.04	1.02	0.07	2020	5	960	10	nd
E2_2_III-H2	A and B	57	20.95	0.95	-11.37	0.02	0.22	0.06	2026	2	960	10	nd
E7_2_II-SB	A and B	48	nd	nd	-12.44	0.16	-0.85	0.17	2021	28	960	10	10
E4_3-H2	A	90	6.51	0.13	-11.11	0.02	1.15	0.06	2040	5	920	10	nd
E2_3_II-H2	A and B	87	19.00	0.22	-12.04	0.01	0.22	0.06	2025	3	920	10	nd
E7_3-SB	A	56	nd	nd	-13.10	0.17	-0.84	0.17	2007	29	920	10	10

238   "nd" = not determined.

239   [a]Starting material (see Table 1).

240   [b]fH$_2$ determined by bracketing PH$_2$; values are the average of the minimum and maximum pressures recorded during the run. See text
241   for details.

242   [c]Uncertainty in fH$_2$ equals half the range of PH$_2$ (max-min).

243 [d]Propagated uncertainty based on uncertainty in fH_2, T and P using the water break down
244 reaction with the equation of states of Churakov and Gottschalk (2003). For SB-runs, error
245 propagation was based on the corresponding buffer equations (Frost 1991; Pownceby and
246 O'Neill 1994). Conversion into ΔFMQ follows Ballhaus et al. (1991).

247 [e]Uncertainty in P is determined as for PH_2.

248 [f]Uncertainty in T from the temperature gradient along capsule lengths or from temperature
249 cycling (T_{cyc}).

250

3. Analytical Methods

3.1. Sample preparation and backscattered electron (BSE)-imaging

253 After the experiments, all capsules were checked for conservation of mass.

254 Consecutively, the capsules were pierced and checked for the presence of excess water

255 visually and by heating them to 120 °C for 30 minutes and monitoring the weight loss during

256 the process. The capsules were then vacuum-impregnated and embedded in epoxy resin

257 and subsequently ground until sufficient run product material was exposed. This process

258 was followed by polishing and carbon coating. The run products were first characterized by

259 back scattered electron (BSE) imaging by using a Jeol JSM 7001F Scanning Electron

260 Microscope. It served as a qualitative assessment of the textural distribution of different

261 mineral phases and their identification. All pieces of analytical instrumentation utilized in

262 this study are housed within the Department of Earth Sciences at the University of Geneva.

3.2. Electron probe microanalysis (EPMA)

264 Major and minor element concentrations (Si, Al, Ca, Mg, Fe, Na, K, Mn, Ti, P, Ni, and

265 Cr) were determined by using a JEOL JXA-8200 Superprobe or later a Hyperprobe-JXA-

266 IHP200F electron microprobe, utilizing wavelength dispersive spectrometers at an

267 acceleration voltage of 15 kV. A beam current of 6 nA, accompanied by a spot size of 10 μm

268 for the glass matrix, and 20 nA with a spot size of < 1 μm for mineral phases, were applied.

269 Calibration of olivine and glass analyses were done by using various natural mineral and

270 glass standards (glass Smithsonian A99 for Si and Al; olivine for Si and Mg; fayalite for Fe;

271 albite for Na; wollastonite for Ca; orthoclase for K and Al; apatite for P_2O_5; nickel oxide for

272 Ni; chromium oxide for Cr; and $MnTiO_3$ for Mn and Ti). Peak and background measurements

273   for all elements were set at 30 s and 15 s, respectively. To mitigate alkali loss, these were

274   reduced to 20 and 10s for Na and K while measured first on respective detectors. In the

275   case of olivine analysis, Al, Ti, and Ca were corrected for secondary fluorescence effects

276   after the method of Gavrilenko et al. (2023) assuming an average grain radius of 10 μm.

277   Secondary reference materials such as San Carlos olivine and the Smithsonian volcanic

278   glasses VG2 and ML3BG were employed to ascertain the results' accuracy and precision.

279   For further analytical details see supplementary material (Table S.3 - S.7 and

280   Figure S.2 and 3). In addition, element maps were acquired by wavelength-dispersive X-ray

281   electron probe microanalysis (WDX-EPMA) at 15 kV, 20 nA, using a focused beam and dwell

282   time of 350 ms and processed using XMapTools 4.3 (Lanari et al., 2014, 2019).

283   **3.3. Laser ablation inductively coupled plasma mass spectrometry (LA-ICP-MS)**

284   *3.3.1. Data acquisition*

285   The LA-ICP-MS analysis was performed using an ESL-193 HE laser ablation system

286   from coupled to an Agilent 8900 triple quadrupole ICP-MS. The nebulizer gas (Ar) and a

287   carrier gas (He) flow rates for were 0.85 ± 0.02 l/min and 0.85 l/min, respectively. The

288   instrument was tuned to ThO/Th ≤ 0.3 %, mass-21/mass-42 ~0.2 % and 238U/232Th of ~1.0

289   using the glass reference material NIST610. The USGS basaltic glass standard GSD-1g was

290   used as an external standard, whereas NIST610 was measured in each analysis block for

291   quality control. In addition, glass reference material NIST617 was analyzed to correct for

292   the contribution of the polyatomic interference $^{29}Si^{16}O$ to the ^{45}Sc signal. Run product

293   glasses were ablated at an energy density of ~3 J/cm^2, a repetition rate of 7 Hz and a laser

294   spot size of 30 μm. Each acquisition consisted of 35 s of background collection followed by

295   40 s of signal counting time. Mineral phases were ablated at an energy density of ~2 J/cm^2

296   and a repetition rate of 4 Hz. The laser spot size was from 7 to 10 μm and the signal duration

297   varied from 2 to 30 s. On-peak dwell times were set to 10 ms for most isotopes. For olivines

298   the dwell times were increased for certain elements (see Table S.5). Each analysis block

299   consisted of ~35 analyses of unknowns bracketed by two measurements of GSD-1g and one

300   measurement of each NIST610 and NIST617. Due to small crystal sizes in the run products,

301   the signals can be short (e.g., ~2 s) or represent a mixture of the mineral phase and the

302 glass matrix. Because Cs, Nb, Th and U are highly incompatible in olivine, they were used

303 as proxies to identify and exclude signal contamination from glass matrix ablation

304 (Nandedkar, 2014).

305 *3.3.2. LA-ICP-MS data processing*

306   The raw data of olivine and glass were first cleaned for signal spikes by an in-house

307 Python algorithm. Data from olivine and glass analyses were processed using the SILLS

308 program (Guillong et al., 2008) and the Iolite software (Paton et al., 2011), respectively.

309 Limits of detection (LOD) calculations followed the method of Longerich et al. (1996). Based

310 on the NIST617 analysis, the contribution of the polyatomic interference $^{29}Si^{16}O$ to ^{45}Sc

311 signal was corrected (typically about 1 µg/g artificial signal on Sc) similar to the method of

312 Jenner and O'Neill (2012). Olivine quantification used 100 wt.% major element oxide total

313 as internal standard, while glass quantification used Silicon (^{29}Si) from EPMA measurements

314 (SiO_2) as the internal standard. For glass analysis, LA-ICP-MS signal intervals (~20 s)

315 excluded significant Cr spikes and plateaus, which resulted from small spinel crystals within

316 the ablated glass volume. For olivine, only signal intervals free of proxy elements for glass

317 contamination were chosen as schematically summarized in Fig. 1. Analyses showing clear

318 downhole elemental fractionation were omitted. Concentrations are reported as geometric

319 means ± standard errors (1σ) from valid measurement spots. However, these values may

320 still reflect sampling biases in olivine signal intervals, as the small spot size increases

321 susceptibility to downhole elemental fractionation over acquisition time. A more accurate

322 approach is to apply a signal stitching technique on the raw spectra to form a composite

323 sample signal of multiple individual sampling intervals similar to the approach of

324 Rauchenstein-Martinek et al. (2014). To carry out the raw signal stitching, an in-house

325 developed Python algorithm was applied (schematically illustrated in Figure S.4). The

326 stitched signal for each sample was processed using the SILLS program, selecting only

327 segments free from downhole elemental fractionation and employing the same standard

328 blocks as in the conventional approach. This procedure also allows the exclusion of false

329 positive sample intervals (i.e., spinel inclusions) from the signal integration. The resulting

330 uncertainties on concentration values are solely analytical. This approach improves counting

14

331 statistics, lowers detection limits, and in most cases yields smaller uncertainties compared

332 to the sample variance derived from conventional data processing. The resulting contents of

333 representative elements for both conventional and stitched signal integration are within

334 10 rel.% (Figure S.5). Due to the increased precision and accuracy, the data obtained by

335 the signal stitching procedure are used for interpretation. For detailed information about

336 precision and accuracy assessment of olivine and silicate glass see Table S.5,

337 Figure S. 6 - S.9.

3.4. Raman spectroscopy

339   Confocal Raman microspectrometry was applied to quantify the water content in the

340 run product glasses. Raman spectra were collected using a confocal LabRAM HR Evolution

341 (HORIBA Scientific) Raman spectrometer with an 800 mm focal length. The spectral

342 resolution was ~0.5 cm^{-1}. A grating of 600 lines/mm and a confocal hole of 100 μm were

343 employed. A 100 mW Toptica TopMode 405 laser source (Toptica Photonics) with a

344 wavelength of 405 nm was used for excitation. The spectra were acquired in backscattering

345 geometry using an Olympus LMPlanFLN 50X long working distance objective. For each

346 spectrum, three accumulations of 30 s each were taken in the spectral window of

347 50 – 4000 cm^{-1}. To prevent laser heating-induced damage to the glass, the laser energy on

348 the sample surface was reduced to about 2 mW by using a density filter. The Raman

349 spectrum was quantified using SilicH2O (van Gerve and Namur, 2023). Reference materials

350 included two andesitic glasses (#159 and #155), containing 5.74 and 5.54 wt.% water,

351 respectively, measured by FTIR (Zajacz et al., 2005, 2012), and an in-house water-free

352 glass.

3.5. QEMSCAN and ImageJ

354   To obtain a quantitative assessment of mineral proportions, an automated mineral

355 analysis and textural imaging were performed using a FEI QEMSCAN® Quanta 650F facility.

356 The system is equipped with two Bruker QUANTAX light-element energy dispersive X-ray

357 spectrometer (EDS) detectors. Analyses were conducted at high vacuum, accelerating

358 voltage of 25 kV, and a beam current of 10 nA on carbon-coated polished epoxy mounts.

359 Analyses were performed in Field-Image mode (Pirrie et al., 2004). In total, between 9 and

360 15 individual fields were measured per sample, with 1000 μm per field, and point spacing of

361 1 μm. The standard 1000 counts per point were acquired, yielding a limit of detection of

362 approximately 2 wt.% per element for mineral classifications. Measurements were performed

363 using iMeasure v5.3.2 software, and data processing using the iDiscover® v5.3.2 software

364 package. The final results consist of: 1) high-quality spatially resolved and fully quantified

365 mineralogical maps; 2) BSE images with identical resolution as the mineralogical maps; 3)

366 X-ray element distribution maps. The results of QEMSCAN analysis were compared with

367 those obtained using ImageJ (Schindelin et al., 2012) applied to the BSE image overviews

368 acquired via SEM imaging (section 3.1). Due to similarities in contrast and brightness, the

369 ImageJ algorithm cannot reliably distinguish between different ferromagnesian minerals,

370 between the glass matrix and plagioclase, or between spinel and apatite. Therefore, the

371 ImageJ-based analysis serves primarily as a secondary assessment of mineral proportions,

372 particularly given that the QEMSCAN analysis was performed on a reduced area compared

373 to the full sample surface and carries higher uncertainties for very small mineral grains (e.g.,

374 spinel and apatite) due to single-pixel resolution limits.

375 **3.6. Statistical analysis and error propagation**

376 In this study, the distribution of geochemical data as a function of experimental

377 parameters (P, T, X, and fO_2) was evaluated using linear and non-linear regression in

378 OriginPro (OriginLab, 2024), employing iterative least squares via the Levenberg–Marquardt

379 algorithm (Marquardt, 1963; Moré, 1978). Model fit significance was assessed by p-values

380 for each parameter estimate (e.g., slope, intercept, inflection point, or asymptote), testing

381 the null hypothesis that the parameter equals zero (i.e., that the model fit is not significantly

382 different from a simpler baseline). A p-value below 0.05 (rejection of null hypothesis)

383 indicates statistical significance with a default display cutoff of 0.0001. The fitting procedure

384 was considered converged at a X^2-tolerance of $1*10^{-9}$. OriginPro automatically generates

385 1000 interpolated points to plot smooth fitted curves. Fit quality is expressed by the

386 coefficient of determination (R^2) and the root mean squared error (RMSE) values. In addition,

387 principal component analysis (PCA) and a correlation matrix (CorMat) were applied to log-

388 normalized geochemical dataset to explore parameter relationships and identify underlying

389 correlations.

390 The bulk partition coefficient of heterovalent elements as a function of fO_2 is known

391 to follow a sigmoidal trend (Mallmann et al., 2022), where the central portion of the curve

392 can be approximated by a linear regression. However, sigmoidal fitting is sensitive to

393 uncertainties in the top and bottom asymptotes. While these asymptotes are mathematically

394 essential for defining the full sigmoidal function, they correspond to fO_2 where the calibrated

395 oxybarometer is not typically applied. To reduce the impact of these uncertainties on the key

396 parameters of interest (i.e., the curve center and slope), a two-step sigmoidal fitting

397 approach was used: 1) An initial exploratory sigmoidal fit was performed. Due to the limited

398 availability of experimental data at extreme fO_2 conditions (outside FMQ -5 to +5, c.f.

399 Erdmann et al. (2024)), this step often yielded high uncertainties in the asymptote estimates,

400 which dominated the total fitting uncertainty (c.f. Motulsky and Christopoulos, 2004). 2) In

401 the second fitting step, the top and bottom asymptotes were fixed to the values obtained in

402 the primary fit, using their 95% confidence intervals. This constraint allowed for a more

403 robust estimation of the central parameters, and the remaining uncertainties were

404 subsequently incorporated into the error propagation for each oxybarometer calibration.

405 For error propagation (standard error, SE) we provide the equations for linear and sigmoidal

406 functions as follows:

407   1) For linear function:

$$\text{1SE Uncertainty } (\Delta FMQ)$$
$$= \sqrt{(\Delta y/m)^2 + \left(\left[-(y-t)/m^2\right]*\Delta m\right)^2 + (-\Delta t/m)^2} \quad (1)$$

409 The variables denote the respective parameters in the linear equation $y = m*x + t$, where y

410 represents the partition or exchange coefficient, t is the intercept, m is the slope, and Δ

411 corresponds to the 1σ uncertainty of each parameter.

412   2) For sigmoidal function:

$$
\text{1SE Uncertainty } (\Delta FMQ)
$$

$$
= \sqrt{(\Delta LOGx0)^2 + \left(\frac{\sqrt{\left[\frac{\sqrt{\Delta A2^2 + \Delta A1^2}}{y - A1} \right]^2 + \left[\frac{(A2 - A1) * \Delta y}{(y - A1)^2} \right]^2 + \left[\frac{(A2 - A1) * \Delta A2}{(y - A1)^2} \right]^2}}{\left[\left(\frac{A2 - A1}{y - A1} \right) - 1 \right] * \ln(10) * p} \right)^2 + \left(\left[\frac{\log_{10}\left[\left(\frac{A2 - A1}{y - A1} \right) - 1 \right]}{p^2} \right] * \Delta p \right)^2 } \quad (2)
$$

414   The variables denote the respective parameters in the sigmoidal function

415    $y = A1 + \left((A2 - A1) \Big/ \left[1 + 10^{(LOGx0 - x) * p} \right] \right)$, where y represents the partition or exchange coefficient,

416    $LOGx0$ the center, p the hill slope and x the logfO_2 (ΔFMQ). $A1$ and $A2$ are the bottom and

417   top asymptote, respectively. Δ-notation indicates the 1σ uncertainty of each parameter.

418   After defining individual oxybarometers through regression fitting, their performance

419   was evaluated using two criteria: 1) The propagated uncertainty: The total uncertainty

420   (combining both fitting and analytical components) was assessed as the median propagated

421   uncertainty across the calibration dataset. This approach reduced the influence of outliers

422   with exceptionally high analytical uncertainty. 2) The reproducibility of the calibration

423   dataset: The predictive success of each oxybarometer can be estimated by the percentage

424   of calibration data points it can reproduce within a defined fO_2-threshold of 0.5 ΔFMQ. This

425   threshold reflects the typical combined uncertainties associated with experimental fO_2

426   measurements and model predictions in high-temperature magmatic systems (Erdmann et

427   al., 2024). A prediction was considered successful if the difference between the calculated

428   fO_2 (including its 2σ propagated uncertainty) and the measured fO_2 (including 2σ uncertainty

429   on fO_2 control of 0.2 ΔFMQ, if not defined otherwise) was less than the 0.5 ΔFMQ threshold

430   value.

431   The performance of both published and newly developed oxybarometers was

432   evaluated by comparing calculated and measured fO_2 values. Hereby, two parameters were

433   used to quantify their performance: 1) Pearson's R^2 for an assessment of precision (Prec.)

434   and 2) the proximity to the line of equality (equiline) valuing the accuracy (Acc.) of

435   reproducing the measured fO_2. Precision and accuracy assessment were combined by using

436 the so-called concordance correlation coefficient (CCC, Lawrence, 1989) together with the

437 RMSE. The CCC ranges from 0 to 1, with values closer to 1 indicating better model

438 performance. In addition, the 2σ propagated uncertainty (Unc.) for each oxybarometer was

439 evaluated as well.

4. Results

4.1. Quality control measures

442   This section overviews essential prerequisites of successful experiments, addresses

443 limitations, and assesses the quality of fO_2 control during experiments. Experiments are

444 considered successful if the following requirements are fulfilled: 1) the mass of experimental

445 capsules is conserved; 2) the presence of excess water is confirmed; 3) stable redox

446 conditions are attained throughout the experimental run; 4) a chemically closed system is

447 maintained (i.e., negligible Fe-loss); and 5) the run product glass and olivines are chemically

448 homogeneous.

449   The masses of the inner and double capsules were measured before and after the

450 experimental runs, revealing no significant differences for most of the experiments (Table

451 3). As all experimental capsules were filled with abundant distilled water (around 10 wt.%),

452 fluid bubbles observed as cavities, are considered as an effect of excess water trapped in

453 the viscous melt-crystal mush upon quenching (Marxer et al., 2021). Raman spectrometry

454 applied on the run product glasses (Table 3) results in water concentrations consistently

455 around 5.5 wt.% and corresponds well to the expected values at water saturation at the

456 experimental run conditions (T = 1019-920 °C and P = 200 MPa (Lesne et al., 2011;

457 Botcharnikov et al., 2015)). This confirms that water in the excess fluid phase was not

458 significantly diluted by other volatile species such as N_2 and CO_2 and therefore the activity

459 of water can be considered equal to 1.

460   Water-saturated conditions facilitate precise control of fO_2 via the imposed hydrogen

461 during experiments, with key parameters being fluctuations in PH_2, pressure (i.e., PAr), and

462 temperature. Except for PH_2, the same applies to SB-runs. The combination of these key

463 parameters allows obtaining a propagated uncertainty on the imposed fO_2 as listed in Table

464 2. For all experiments, logfO_2 uncertainty was < 0.20 log units (ΔFMQ), except for two runs

465 (E1.1_IV_H2 and E5.2_H2), which showed higher uncertainties of ~0.4 log-units. For

466 E1.1_IV_H2, notable PH_2 fluctuations were observed, while E5.2_H2 was subject to

467 temperature-cycling (±15 °C).

468   Maintaining a chemically closed system is essential for successful experiments.

469 Potential Fe-loss to the Au-capsule and the occurrence of cryptocrystalline to amorphous

470 aggregates of residual powder linked to hercynitic spinel formation are key concerns. Iron

471 loss was estimated through optimized mass balance regression, combining BSE-derived

472 estimates for mineral proportions with their EPMA-based compositions. Table 3 shows that

473 values for the Fe-loss (ΔFe_{loss} in rel.%) are in general below 5 % relative to the bulk FeO

474 content of the starting material except for most reducing runs (CCO-buffer, ≤ 13 rel.% Fe-

475 loss). The sum of the squared residuals from the mass balance calculation (ΣR^2) shows

476 mostly values below 1, except for one experiment (Table 3). For further details regarding

477 the mass balance calculation see Table S.8. Overall, we conclude that due to the applied

478 low temperature ($T \leq 1020$ °C) and the use of pure Au-capsules for all runs (except

479 E7.0_II_SB), Fe-loss does not significantly impact the fractional crystallization series in this

480 study.

481   In two-thirds of the experiments, we observed minor patches of unreacted powder

482 associated with hercynitic spinel which appears to be sealed off from the actual experimental

483 load by overgrown plagioclase. This experimental artifact is referred to as residual powder

484 artifact (RPA). It is considered negligible, as no systematic correlation is observed between

485 their presence and any intensive parameter (i.e., fO_2) or chemical variable (e.g., the V-Sc-,

486 Fe-Mg exchange and V partition coefficient between olivine and melt), nor do they influence

487 the LLD. Statistical analysis, including a CorMat and conditional density plots with RPA as

488 a categorical factor, revealed no significant relationships. While conditional density plots

489 suggest slightly more frequent RPA occurrence at lower temperatures, the correlation matrix

490 showed no meaningful correlation (see Figure S.10 and Table S.9). For example, in

491 experiment E4_2_H2_II_B, optimized mass balance calculations yielded a good fit

492   (ΣR^2 = 0.90). The estimated mineral proportions (in rel.%) are glass (Gl): 94.00, olivine (Ol):

493   3.08, Pl: 2.44, spinel (Spl): 0.16 and apatite (Ap): 0.32. These values align with those

494   obtained from QEMSCAN (Gl: 94.88, Ol: 2.34, Pl: 2.73, RPA: < 0.10, Spl+Ap < 0.10) and

495   ImageJ combined (Gl+Pl: 96.24, Ol+RPA: 3.20, Spl+Ap: 0.57). For detailed information see

496   supplementary material (Table S.10 and Figure S.11). The mineral proportions derived from

497   optimized mass balance, QEMSCAN and imageJ collectively support the statistical evidence

498   that RPA presence does not affect the LLD. In addition, all experiments showed residual

499   liquid being quenched to a homogeneous glass (c.f. Table 4 and subsequent section).

500   **4.2. Attainment of equilibrium**

501   The attainment of equilibrium was mainly assessed by time series experiments at

502   constant fO_2 (FMQ +2.5), T = 960 °C and P = 200 MPa and variable run duration (28, 56,

503   and 106 h) including a comparison of SB- (i.e., ReReO$_2$) with H$_2$-runs. As shown in Fig. 2

504   the Fe-Mg and V-Sc exchange coefficients are consistent within 2σ standard error

505   independent of run duration. Only the MKCA sample at the shortest run duration falls outside

506   the 2σ range. All experiments were carried out at a significantly longer run duration than

507   28 h, except for E7.0_II_SB (18 h, 1019 °C, FMQ -0.87) to prevent the exhaustion of the

508   CCO buffer. The run duration was increased with decreasing temperature (Table 2). The

509   homogeneity of run product glasses and olivines serves as secondary indication of reaching

510   chemical equilibrium. Element distribution maps for the redox-sensitive element Fe

511   demonstrate chemical homogeneity, confirming the attainment of redox equilibrium (Fig. 3).

512   Due to its fast diffusion under magmatic conditions it is sensitive to detect any redox

513   disequilibrium (Shea et al., 2023).

514   **4.3. Experimental run products**

515   *4.3.1. Textural and phase assemblage overview*

516   Olivine crystallizes alongside various other minerals (according to their frequency of

517   occurrence: spinel, plagioclase, clinopyroxene (Cpx), apatite, orthopyroxene (Opx),

518   amphibole (Amp), ilmenite (Ilm) and phlogopite (Phl)). Regarding glass and olivine, all major-

519   (i.e., FeO), minor- and most trace elements (i.e., V) show low variations (Tables 4 and 5).

520 In general, olivine occurs as subhedral crystals with rounded margins containing

521 occasionally spinel and/or plagioclase inclusions. The olivine stability field at 920 °C seems

522 to be restricted to fO_2 between FMQ -0.86 and FMQ +1.25, and preferably for MKCA starting

523 material. Only for this starting material, the E7.X_SB-fO2- series (approx. FMQ -0.87)

524 showed olivine at four distinct temperatures (1019, 990, 960, and 920 °C). Therefore, we

525 use these experiments to highlight the textual relationship between olivine and co-

526 crystallizing mineral phases as a function of temperature, as summarized in Fig. 4.

527 Especially in experiment E7.3_SB_A (920 °C) the olivine appears only in very small amounts

528 and reduced crystal size.

529 Table 3 Summary of run products: water content, residual powder artifact (RPA), and relative
530 Fe-loss.

Sample	[a]ΔFe-loss-%	[a]ΣR^2	[b]RPA	[c]Δ-mass$_{cap}$ (mg)	[c]Δ-mass$_{dried}$ (mg)	[d]H_2O (wt.%)	[d]$\pm\Delta$ H_2O (wt.%)
E7.0_II_SB_A	10.43	0.41	x	0.04	2.28	5.51	0.16
E7.0_II_SB_B	10.62	0.37	o	0.04	2.34	5.53	0.16
E1.1_IV_H2_A	8.18	0.24	x	0.18	1.4	6.37	0.31
E1.1_IV_H2_B	3.37	0.11	o	0.02	1.43	5.31	0.24
E3.1_II_SB_A	1.18	0.00	x	nd	0.81	5.50	0.15
E3.1_II_SB_B	0.14	0.69	o	-1.1	1.84	5.46	0.17
E4.1_IV_H2_A	4.14	0.00	o	0	1.48	5.31	0.17
E4.1_III_H2_B	0.27	0.00	o	-0.01	1.49	5.75	0.17
E4.1_IV_H2_B	6.18	0.02	o	-0.01	1.53	5.76	0.17
E2.1_III_H2_A	3.23	0.21	x	-0.05	1.33	6.05	0.15
E2.1_III_H2_B	1.40	[e]3.76	o	-0.08	1.41	6.51	0.19
E7.1_SB_II_A	12.15	0.01	o	nd	nd	6.93	0.16
E7.1_SB_II_B	12.77	0.64	o	nd	1.5	6.95	0.17
E1.2_H2_A	1.19	0.30	x	0	1.17	5.50	0.76
E1.2_H2_B	3.70	0.09	x	-0.02	1.22	6.69	0.37
E3.2_SB_A	3.00	0.08	x	nd	0.48	5.79	0.16
E3.2_II_H2_A	4.08	0.75	x	0.01	1.21	5.49	0.23
E3.2_SB_B	0.24	0.00	o	nd	1.98	5.62	0.20
E3.2_II_H2_B	0.91	0.01	x	-0.01	1.3	6.20	0.16
E3.2_IV_H2_B	0.15	0.16	x	0.02	1.29	6.81	0.20
E5.2_H2_A	0.69	0.24	o	nd	1.31	5.71	0.17
E4.2_II_H2_A	3.29	0.28	o	-0.03	1.44	6.60	0.30

531

532   Table 3. (continued).

Sample	[a]ΔFe-loss-%	[a]ΣR^2	[b]RPA	[c]Δ-mass$_{cap}$ (mg)	[c]Δ-mass$_{dried}$ (mg)	[d]H$_2$O (wt.%)	[d]±Δ H$_2$O (wt.%)
E4.2_H2_B	5.55	0.39	o	-0.06	1.34	6.46	0.17
E4.2_II_H2_B	2.46	0.90	x	-0.1	1.26	6.32	0.16
E2.2_III_H2_A	3.18	0.04	o	0.08	1.28	6.71	0.19
E2.2_III_H2_B	2.10	0.46	o	0.01	1.45	7.44	0.18
E7.2_II_SB_A	10.75	0.02	x	-0.06	0.32	7.15	0.17
E7.2_II_SB_B	10.61	0.19	x	0.01	1.13	6.46	0.17
E2.3_II_H2_A	11.30	0.21	o	-0.03	1.32	7.36	0.34
E2.3_II_H2_B	4.93	0.02	x	-0.02	1.36	8.00	0.37
E7.3_SB_A	11.18	0.56	x	0.25	2.74	7.42	0.22

533   "nd" = not determined.

534   [a]Relative Fe-loss (%) from mass balance regression; ΣR^2 gives the sum of squared residuals.
535   Details in supplement tables, Table S.8 - S.10).

536   [b]Rresidual starting powder (RPA) detected (x) or not detected (o).

537   [c]Δ-m$_{Cap}$ and Δ-m$_{-dried}$ are changes in capsule mass during the experiment and after
538   piercing/drying, respectively. "nd" indicates the capsule was not recovered intact. Capsule
539   integrity confirmed by residual water.

540   [d]H$_2$O contents by Raman spectroscopy with propagated 1σ standard deviation (SD).
541   Elevated values in some glasses may reflect systematic overestimation due to baseline
542   correction artifacts.

543   [e]Outlier of mass balance calculation, which is traced back to a misfit for Ca and Si, potentially
544   due to undetected clinopyroxene.

545

546   *4.3.2. The chemical composition of run product glass and olivine*

547   Comparing the geometric mean (μ$_{[geo.]}$) with its sample variation (standard

548   deviation, 1σ SD) serves as an indicator for the homogeneity of both glass (Table 4) and

549   olivine (Table 5). Hereby, the median value of the coefficient of variation (CV [%]

550   = 1SD)/μ$_{[geo.]}$ x100) is used (Stanley and Lawie, 2007). Glass composition demonstrates

551   generally low values for all major (< 3 %) and minor (< 13 %) elements. For most of the trace

552   elements, the CV is below 10 %, with a few exceptions for Cr and Ni (Table S.6. and S.11).

553   In the run product glasses, FeO varies from 3.00±0.02 to 7.05±0.03 wt.%, and MgO from

554   1.60±0.01 to 4.51±0.02 wt.%, both decreasing with decreasing temperature. Vanadium

555   ranges from 80.0±1.0 to 320.0±4.0 µg/g, and Sc from 24.7±0.8 to 59.5±1.2 µg/g.

556   In olivine, the CV values for all major-, minor- and most trace elements are mostly

557   below 2, 10 and 20 % respectively. Only samples E7.3_SB_A and E3.2_II_B show higher

558   values for some trace elements (Na, P, Cr, Ti, Yb and Ga, Table S.4, S.7. and S.12). Besides

559   the perspective of point analysis, element distribution maps were acquired on olivines for

560   representative samples as outlined in subsection 4.3.1. The most sensitive elemental redox

561   proxies (i.e., Fe) demonstrate no significant chemical zonation (Fig. 3). FeO content in

562   olivine range from 8.60±0.01 to 26.11±0.11 wt.%, while V-content varies from 1.9±0.1 to

563   35.1±2.2 µg/g. For both elements, their content increases with decreasing fO$_2$, and to a

564   lesser extent with decreasing temperature. The corresponding values of MgO range from

565   34.19±0.10 to 49.56±0.11 wt.%. Scandium varies between 11.8±0.5 and 70.1±4.8 µg/g and

566   shows a very weak positive correlation with decreasing temperature which is associated with

567   an increase in polymerization of the silicate melt (i.e., non-bridging oxygens per tetrahedrally

568   coordinated cation, NBO/T).

569

570   Table 4 Composition of the glass run product (including Sc, V, Cs and U).

Sample	[a]SiO$_2$ (wt.%)	[a]TiO$_2$ (wt.%)	[a]Al$_2$O$_3$ (wt.%)	[a]FeO (wt.%)	[a]MnO (wt.%)	[a]MgO (wt.%)	[a]CaO (wt.%)	[a]N$_2$O (wt.%)	[a]K$_2$O (wt.%)	[a]P$_2$O$_5$ (wt.%)	[a]Total (wt.%)	[a]n	[b]Sc µg/g	[b]V µg/g	[b]Cs µg/g	[b]U µg/g	[b]n	[c]NBO/T
E7.0_II_SB_A	50.00	1.17	18.13	6.30	0.18	4.51	9.42	2.97	0.79	0.31	93.78	29	45.9	250	102	27.2	14	0.608
	(0.07)	(0.01)	(0.06)	(0.09)	(0.01)	(0.02)	(0.02)	(0.03)	(0.01)	(0.02)	(0.2)		(0.91)	(3.1)	(0.51)	(0.18)		0.554
E7.0_II_SB_B	50.29	1.22	17.17	6.14	0.24	3.86	7.78	3.20	3.21	0.89	94.00	35	45.2	263	115	30.8	15	0.344
	(0.05)	(0.01)	(0.04)	(0.05)	(0.01)	(0.02)	(0.02)	(0.02)	(0.02)	(0.02)	(0.07)		(0.5)	(2.08)	(0.48)	(0.32)		0.335
E1.1_IV_H2_A	56.35	1.24	17.99	3.50	0.16	3.36	6.23	3.88	0.99	0.44	94.15	35	59.5	320	114	29	12	0.451
	(0.03)	(0.01)	(0.02)	(0.02)	(0.01)	(0.01)	(0.02)	(0.02)	(0.01)	(0.01)	(0.04)		(1.16)	(3.72)	(0.91)	(0.32)		0.418
E1.1_IV_H2_B	54.20	1.03	19.44	3.11	0.18	3.32	6.23	3.62	2.33	0.86	94.31	35	50	270	93.2	25.2	13	0.508
	(0.04)	(0.02)	(0.02)	(0.02)	(0.01)	(0.01)	(0.02)	(0.02)	(0.01)	(0.02)	(0.05)		(1.05)	(2.51)	(0.45)	(0.17)		0.496
E3.1_II_SB_A	53.59	1.07	17.67	4.94	0.19	3.88	7.27	3.50	0.76	0.39	93.27	44	51	265	95.2	24.7	17	0.472
	(0.05)	(0.01)	(0.05)	(0.04)	(0.01)	(0.02)	(0.01)	(0.02)	(0.01)	(0.01)	(0.08)		(0.63)	(1.66)	(0.5)	(0.18)		0.606
E3.1_II_SB_B	52.91	0.99	18.30	4.58	0.14	3.59	6.50	3.68	2.41	0.98	94.05	45	50.1	260	88.7	24.4	14	0.560
	(0.03)	(0.01)	(0.03)	(0.04)	(0.01)	(0.02)	(0.01)	(0.02)	(0.01)	(0.02)	(0.08)		(0.67)	(0.82)	(0.56)	(0.12)		0.503
E4.1_IV_H2_A	52.18	0.99	18.09	6.73	0.14	3.74	7.76	3.14	0.80	0.33	93.90	30	42.1	251	108	30.1	14	0.464
	(0.04)	(0.02)	(0.05)	(0.03)	(0.01)	(0.02)	(0.04)	(0.01)	(0.01)	(0.01)	(0.06)		(1.11)	(1.94)	(1.01)	(0.27)		0.608
E4.1_III_H2_B	51.34	1.11	17.79	6.33	0.13	3.59	7.17	2.90	2.66	0.86	93.86	44	37.1	239	101	26.5	13	0.554
	(0.03)	(0.01)	(0.02)	(0.02)	(0.01)	(0.01)	(0.03)	(0.01)	(0.01)	(0.01)	(0.05)		(0.48)	(9.1)	(2.29)	(0.6)		0.344
E4.1_IV_H2_B	51.87	1.12	18.05	6.03	0.12	3.46	7.09	2.93	2.66	0.86	94.17	30	31.1	222	92.2	23	14	0.335
	(0.03)	(0.02)	(0.02)	(0.03)	(0.01)	(0.02)	(0.01)	(0.02)	(0.01)	(0.01)	(0.05)		(0.28)	(1.7)	(0.73)	(0.15)		0.451
E2.1_III_H2_A	50.13	1.06	18.25	7.05	0.18	4.49	8.94	2.96	0.65	0.37	94.10	30	49.4	260	95	23.7	14	0.418
	(0.03)	(0.02)	(0.02)	(0.03)	(0.01)	(0.01)	(0.02)	(0.01)	(0.01)	(0.01)	(0.05)		(0.38)	(1.93)	(0.52)	(0.2)		0.508
E2.1_III_H2_B	49.87	1.31	17.80	7.05	0.15	3.98	7.45	3.23	2.45	0.95	94.22	30	51.4	258	89.1	23.1	13	0.496
	(0.03)	(0.02)	(0.02)	(0.03)	(0.01)	(0.01)	(0.02)	(0.02)	(0.01)	(0.02)	(0.04)		(0.5)	(1.4)	(0.25)	(0.18)		0.472
E7.1_SB_II_A	51.87	1.39	17.90	5.49	0.21	3.96	8.04	3.26	0.85	0.41	93.40	35	47.4	243	104	26.5	8	0.606
	(0.05)	(0.01)	(0.04)	(0.03)	(0.01)	(0.03)	(0.02)	(0.02)	(0.01)	(0.01)	(0.1)		(0.57)	(1.36)	(0.3)	(0.24)		0.560
E7.1_SB_II_B	52.07	1.40	17.21	5.08	0.26	3.52	7.04	3.11	2.97	0.90	93.58	35	49.3	278	92.6	23.7	8	0.503
	(0.04)	(0.01)	(0.05)	(0.03)	(0.01)	(0.02)	(0.01)	(0.02)	(0.02)	(0.02)	(0.07)		(0.41)	(3.05)	(0.4)	(0.07)		0.464

571

572   Table 4 (continued).

Sample	$^{a}SiO_2$ (wt.%)	$^{a}TiO_2$ (wt.%)	$^{a}Al_2O_3$ (wt.%)	^{a}FeO (wt.%)	^{a}MnO (wt.%)	^{a}MgO (wt.%)	^{a}CaO (wt.%)	$^{a}N_2O$ (wt.%)	$^{a}K_2O$ (wt.%)	$^{a}P_2O_5$ (wt.%)	$^{a}Total$ (wt.%)	^{a}n	^{b}Sc µg/g	^{b}V µg/g	^{b}Cs µg/g	^{b}U µg/g	^{b}n	$^{c}NBO/T$
E1.2_H2_A	57.84 (0.04)	0.96 (0.02)	18.28 (0.03)	3.17 (0.02)	0.13 (0.01)	2.92 (0.01)	5.13 (0.02)	4.05 (0.03)	1.18 (0.01)	0.49 (0.02)	94.14 (0.05)	34	46.5 (0.73)	250 (4.02)	96.8 (0.67)	26.8 (0.38)	11	0.276 0.285
E1.2_H2_B	56.19 (0.04)	1.13 (0.02)	18.54 (0.02)	3.00 (0.02)	0.22 (0.01)	3.01 (0.01)	5.18 (0.02)	3.49 (0.02)	2.50 (0.01)	0.81 (0.02)	94.09 (0.04)	34	53.4 (1.25)	246 (2.94)	102 (0.66)	25.9 (0.45)	12	0.378 0.374
E3.2_SB_A	55.53 (0.13)	1.19 (0.01)	17.11 (0.06)	4.61 (0.02)	0.17 (0.01)	3.28 (0.01)	6.34 (0.01)	3.54 (0.02)	0.66 (0.01)	0.48 (0.02)	92.88 (0.1)	36	47.8 (0.41)	237 (3.23)	95.6 (0.47)	23.7 (0.13)	10	0.356 0.360
E3.2_II_H2_A	55.38 (0.06)	1.10 (0.01)	18.25 (0.04)	4.58 (0.03)	0.16 (0.01)	3.53 (0.02)	6.17 (0.02)	3.70 (0.02)	0.72 (0.01)	0.49 (0.02)	94.10 (0.05)	30	52.7 (0.88)	254 (7.41)	96.1 (0.81)	24.4 (0.25)	18	0.339 0.446
E3.2_SB_B	53.70 (0.15)	0.99 (0.01)	18.31 (0.03)	4.35 (0.01)	0.16 (0.01)	3.16 (0.01)	5.75 (0.01)	3.53 (0.02)	2.06 (0.01)	1.00 (0.02)	93.00 (0.16)	37	49.6 (0.6)	233 (2.21)	89.6 (0.49)	22.8 (0.17)	12	0.440 0.428
E3.2_II_H2_B	53.86 (0.04)	0.95 (0.01)	18.91 (0.03)	4.22 (0.02)	0.15 (0.01)	3.41 (0.01)	5.81 (0.01)	3.53 (0.02)	2.30 (0.01)	0.93 (0.01)	94.08 (0.04)	50	51.3 (1.13)	239 (2.52)	86.6 (0.44)	24.6 (0.36)	11	0.439 0.521
E3.2_IV_H2_B	54.12 (0.03)	0.95 (0.01)	19.13 (0.03)	4.01 (0.02)	0.16 (0.01)	3.23 (0.01)	5.65 (0.01)	3.62 (0.02)	2.37 (0.01)	0.98 (0.02)	94.22 (0.06)	41	53.4 (0.81)	266 (2.51)	102 (0.91)	25 (0.3)	14	0.490 0.276
E5.2_H2_A	53.45 (0.06)	1.08 (0.02)	18.29 (0.08)	5.38 (0.03)	0.20 (0.01)	4.11 (0.02)	6.75 (0.1)	3.40 (0.04)	0.61 (0.01)	0.41 (0.01)	93.71 (0.05)	35	53.5 (1.28)	295 (10.14)	99.8 (2.08)	25.4 (0.48)	6	0.285 0.378
E4.2_II_H2_A	52.94 (0.06)	1.06 (0.01)	18.37 (0.03)	6.20 (0.03)	0.20 (0.01)	3.41 (0.01)	6.66 (0.03)	3.53 (0.02)	1.03 (0.01)	0.42 (0.02)	93.82 (0.08)	40	57.9 (0.86)	267 (2.08)	116 (0.85)	28 (0.59)	11	0.374 0.356
E4.2_H2_B	52.78 (0.05)	1.14 (0.02)	18.22 (0.03)	5.42 (0.03)	0.15 (0.01)	3.32 (0.02)	6.77 (0.02)	2.94 (0.02)	2.53 (0.01)	0.92 (0.02)	94.20 (0.04)	25	45.9 (0.86)	264 (1.98)	82.9 (1.21)	22.2 (0.28)	9	0.360 0.339
E4.2_II_H2_B	52.15 (0.04)	1.13 (0.01)	18.57 (0.02)	5.65 (0.02)	0.15 (0.01)	3.36 (0.01)	6.80 (0.02)	2.95 (0.02)	2.71 (0.01)	0.83 (0.02)	94.32 (0.05)	35	47 (0.48)	279 (2.51)	83.1 (0.34)	22.3 (0.18)	14	0.446 0.440
E2.2_III_H2_A	51.68 (0.04)	1.16 (0.01)	17.49 (0.03)	6.68 (0.03)	0.12 (0.01)	3.82 (0.02)	7.68 (0.03)	3.23 (0.03)	0.71 (0.01)	0.43 (0.02)	93.02 (0.07)	27	50.3 (0.39)	254 (1.52)	95.8 (0.51)	24.6 (0.14)	11	0.428 0.439
E2.2_III_H2_B	51.19 (0.03)	1.43 (0.01)	17.46 (0.02)	6.07 (0.03)	0.12 (0.01)	3.59 (0.01)	7.00 (0.02)	3.09 (0.01)	2.47 (0.02)	0.96 (0.02)	93.38 (0.05)	29	48.9 (0.75)	246 (2.19)	88.9 (0.25)	23.5 (0.23)	10	0.521 0.490

573

574   Table 4 (continued).

Sample	SiO_2 (wt.%)[a]	TiO_2 (wt.%)[a]	Al_2O_3 (wt.%)[a]	FeO (wt.%)[a]	MnO (wt.%)[a]	MgO (wt.%)[a]	CaO (wt.%)[a]	N_2O (wt.%)[a]	K_2O (wt.%)[a]	P_2O_5 (wt.%)[a]	Total (wt.%)[a]	n[a]	Sc µg/g[b]	V µg/g[b]	Cs µg/g[b]	U µg/g[b]	n[b]	NBO/T[c]
E7.2_II_SB_A	55.13	1.58	17.35	4.97	0.17	3.09	6.37	3.70	0.99	0.55	93.89	44	48.9	238	122	30.3	9	0.385
	(0.04)	(0.01)	(0.03)	(0.02)	(0.01)	(0.02)	(0.03)	(0.02)	(0.01)	(0.01)	(0.06)		(1.05)	(5.85)	(0.51)	(0.46)		0.349
E7.2_II_SB_B	54.53	1.29	18.35	4.38	0.20	2.78	5.99	3.49	2.86	0.77	94.63	45	47.1	173	100	26.8	8	0.276
	(0.05)	(0.01)	(0.03)	(0.03)	(0.01)	(0.01)	(0.02)	(0.02)	(0.01)	(0.02)	(0.05)		(1.14)	(2.39)	(0.47)	(0.51)		0.333
E4.3_H2_A	57.99	0.94	17.71	4.56	0.16	2.35	4.83	3.76	1.13	0.52	93.95	45	45.9	152	97.9	29.8	14	0.283
	(0.03)	(0.01)	(0.02)	(0.02)	(0.01)	(0.01)	(0.02)	(0.03)	(0.01)	(0.01)	(0.05)		(0.52)	(1.22)	(1.31)	(0.19)		0.212
E2.3_II_H2_A	56.75	1.07	17.18	5.53	0.15	2.41	5.57	3.54	0.91	0.55	93.66	39	39.9	186	115	33.6	13	0.385
	(0.04)	(0.01)	(0.02)	(0.03)	(0.01)	(0.01)	(0.01)	(0.03)	(0.01)	(0.02)	(0.05)		(1.47)	(1.65)	(0.61)	(0.94)		0.349
E2.3_II_H2_B	56.24	0.99	18.21	4.94	0.13	2.12	4.67	3.46	2.72	0.65	94.12	45	25.1	143	120	34	13	0.276
	(0.04)	(0.01)	(0.02)	(0.02)	(0.01)	(0.01)	(0.02)	(0.02)	(0.01)	(0.01)	(0.04)		(1.43)	(1.15)	(0.3)	(0.63)		0.333
E7.3_SB_A	60.97	0.86	16.15	3.50	0.11	1.60	4.28	3.94	1.34	0.37	93.11	32	24.7	80.3	128	28.9	11	0.283
	(0.07)	(0.01)	(0.03)	(0.04)	(0.01)	(0.01)	(0.01)	(0.03)	(0.01)	(0.01)	(0.04)		(0.76)	(1.05)	(1.19)	(0.31)		0.212

575   "n" = the number of analyses for each analytical technique. Uncertainties are 1σ standard errors (SE) in parentheses. Values below
576   detection limit (BDL) are reported as "< µg/g". Elemental concentrations are rounded according to magnitude and analytical precision.

577   [a]EPMA analysis.

578   [b]LA-ICP-MS analysis.

579   [c]Non-bridging oxygen per tetrahedrally coordinated cation (NBO/T); calculated using Eq. (3) given by Zajacz and Tsay (2019), which is
580   based on Mysen and Richet (2005).

581

582

583

584

585   Table 5 Composition (including Sc, V, Cs and U) of the olivine run phase.

Sample	[a]SiO_2 wt.%	[a]FeO wt.%	[a]MnO wt.%	[a]MgO wt.%	[a]CaO wt.%	[a]Na_2O wt.%	[a]Total wt.%	[a]n	[b]Sc µg/g	[b]V µg/g	[b]Ni µg/g	[b]Cs µg/g	[b]U µg/g	[b]n
E7.0_II_SB_A	38.76 (0.06)	18.32 (0.12)	0.34 (0.01)	43.07 (0.08)	0.20 (0.01)	BDL < 103	100.9 (0.07)	29	15.42 (0.41)	17.47 (0.29)	376.5 (7.79)	BDL < 0.113	0 (0)	21
E7.0_II_SB_B	38.99 (0.1)	19.7 (0.22)	0.6 (0.01)	41.5 (0.16)	0.27 (0.04)	BDL < 104	101.31 (0.09)	13	16.29 (0.9)	16.07 (0.58)	460 (18.01)	BDL < 0.256	0 (0)	16
E1.1_IV_H2_A	40.94 (0.04)	10.23 (0.08)	0.37 (0.01)	48.34 (0.08)	0.11 (0.01)	0.01 (0.01)	100.31 (0.06)	30	14.13 (0.37)	1.88 (0.09)	1438 (10.37)	BDL < 0.118	0 (0)	25
E1.1_IV_H2_B	41.13 (0.06)	8.6 (0.1)	0.48 (0.01)	49.56 (0.11)	0.07 (0.01)	0.02 (0.01)	100.11 (0.07)	28	30.75 (0.58)	2.38 (0.11)	1350 (12.72)	BDL < 0.158	0 (0)	14
E3.1_II_SB_A	40.15 (0.03)	14.33 (0.05)	0.48 (0.01)	45.73 (0.05)	0.12 (0.01)	BDL < 105	101.08 (0.05)	40	13.96 (0.67)	3.21 (0.18)	1274 (16.46)	BDL < 0.281	0 (0)	22
E3.1_II_SB_B	40.4 (0.02)	13.65 (0.03)	0.28 (0.01)	46.25 (0.04)	0.13 (0.01)	BDL < 105	100.99 (0.04)	35	20.58 (0.97)	3.86 (0.26)	1376 (23.12)	BDL < 0.329	0 (0)	20
E4.1_IV_H2_A	39.32 (0.02)	18.39 (0.04)	0.28 (0.01)	41.36 (0.05)	0.17 (0.01)	0.02 (0.01)	99.75 (0.06)	19	11.8 (0.46)	4.1 (0.16)	714.3 (10.88)	BDL < 0.174	0 (0)	20
E4.1_III_H2_B	39.09 (0.03)	17.91 (0.03)	0.27 (0.01)	41.72 (0.03)	0.19 (0.01)	0.02 (0.01)	99.43 (0.04)	31	12.57 (1.2)	3.01 (0.3)	759.3 (22.59)	BDL < 0.279	0 (0)	15
E4.1_IV_H2_B	39.36 (0.03)	18.07 (0.03)	0.28 (0.01)	41.67 (0.03)	0.19 (0.01)	0.02 (0.01)	99.79 (0.04)	21	12.8 (0.6)	3.97 (0.19)	852.4 (13.66)	BDL < 0.227	0 (0)	15
E2.1_III_H2_A	39.08 (0.06)	19.08 (0.05)	0.38 (0.01)	40.59 (0.04)	0.19 (0.01)	0.01 (0.01)	99.51 (0.08)	32	15.53 (0.65)	10.92 (0.22)	475.7 (10.37)	BDL < 0.197	0 (0)	21
E2.1_III_H2_B	38.93 (0.03)	19.94 (0.06)	0.35 (0.01)	39.91 (0.04)	0.21 (0.01)	0.02 (0.01)	99.56 (0.06)	37	18.66 (0.85)	11.35 (0.36)	230.3 (12.25)	BDL < 0.252	0 (0)	13
E7.1_SB_II_A	39.46 (0.04)	17.38 (0.04)	0.45 (0.01)	42.52 (0.13)	0.16 (0.01)	BDL < 104	100.15 (0.17)	22	18.42 (0.98)	13.25 (0.39)	186.9 (8.05)	BDL < 0.33	0 (0)	28
E7.1_SB_II_B	39.44 (0.04)	17.7 (0.09)	0.71 (0.01)	42.28 (0.08)	0.19 (0.01)	BDL < 105	100.5 (0.15)	29	19.9 (1.79)	15.56 (0.71)	458.8 (20.55)	BDL < 0.647	0 (0)	7

586

587   Table 5 (continued).

Sample	[a]SiO$_2$ wt.%	[a]FeO wt.%	[a]MnO wt.%	[a]MgO wt.%	[a]CaO wt.%	[a]Na$_2$O wt.%	[a]Total wt.%	[a]n	[b]Sc µg/g	[b]V µg/g	[b]Ni µg/g	[b]Cs µg/g	[b]U µg/g	[b]n
E1.2_H2_A	40.9 (0.03)	10.93 (0.05)	0.25 (0.01)	47.73 (0.05)	0.08 (0.01)	0.02 (0.01)	100.3 (0.05)	30	23.44 (0.59)	2.84 (0.13)	2322 (15.99)	BDL < 0.126	0 (0)	18
E1.2_H2_B	40.86 (0.03)	10.12 (0.09)	0.53 (0.01)	48.13 (0.06)	0.08 (0.01)	0.01 (0.01)	100.1 (0.04)	28	29 (0.7)	2.67 (0.14)	2528 (18.61)	BDL < 0.148	0 (0)	16
E3.2_SB_A	40.02 (0.03)	14.28 (0.09)	0.4 (0.01)	45.34 (0.11)	0.09 (0.01)	BDL < 109	100.47 (0.06)	30	25.23 (1.27)	4.22 (0.28)	1242 (22.87)	BDL < 0.375	0 (0)	17
E3.2_II_H2_A	40.03 (0.03)	14.55 (0.05)	0.4 (0.01)	44.24 (0.05)	0.13 (0.01)	0.02 (0.01)	99.69 (0.05)	26	21.36 (1.06)	4.13 (0.28)	1862 (32.34)	BDL < 0.315	0 (0)	14
E3.2_SB_B	40.05 (0.04)	14.08 (0.06)	0.42 (0.01)	45.44 (0.08)	0.10 (0.01)	BDL < 110	100.42 (0.1)	29	29.39 (1.65)	4 (0.33)	1518 (31.32)	BDL < 0.487	0 (0)	16
E3.2_II_H2_B	40.25 (0.03)	13.42 (0.03)	0.34 (0.01)	45.14 (0.04)	0.12 (0.01)	0.02 (0.01)	99.66 (0.05)	26	22.97 (1.99)	4.31 (0.5)	1654 (44.68)	BDL < 0.46	0 (0)	20
E3.2_IV_H2_B	40.23 (0.03)	13.36 (0.03)	0.33 (0.01)	45.41 (0.04)	0.09 (0.01)	0.02 (0.01)	99.72 (0.06)	28	23.36 (0.7)	3.64 (0.17)	1500 (16.49)	BDL < 0.152	0 (0)	20
E5.2_H2_A	40.32 (0.05)	14.5 (0.03)	0.45 (0.01)	45.51 (0.04)	0.10 (0.01)	BDL < 104	101.11 (0.05)	33	18.93 (0.58)	3.25 (0.11)	963.4 (9.03)	BDL < 0.19	0 (0)	25
E4.2_II_H2_A	39.14 (0.04)	20.13 (0.1)	0.41 (0.01)	39.81 (0.09)	0.12 (0.01)	0.02 (0.01)	99.8 (0.04)	25	19.72 (0.79)	5.95 (0.24)	642.8 (12.46)	BDL < 0.16	0 (0)	18
E4.2_H2_B	39.11 (0.03)	18.66 (0.05)	0.41 (0.01)	40.92 (0.04)	0.14 (0.01)	0.02 (0.01)	99.46 (0.07)	29	24.04 (0.84)	6.65 (0.25)	777 (14.85)	BDL < 0.169	0 (0)	20
E4.2_II_H2_B	39.42 (0.02)	18.54 (0.03)	0.33 (0.01)	41.11 (0.03)	0.13 (0.01)	0.02 (0.01)	99.77 (0.04)	26	24.13 (0.74)	6.07 (0.21)	763.8 (11.94)	BDL < 0.139	0 (0)	17
E2.2_III_H2_A	38.92 (0.02)	20.8 (0.05)	0.28 (0.01)	40.2 (0.02)	0.15 (0.01)	0.02 (0.01)	100.56 (0.05)	47	16.16 (0.49)	9.58 (0.22)	359.2 (7.84)	BDL < 0.147	0 (0)	23
E2.2_III_H2_B	38.82 (0.03)	19.5 (0.04)	0.31 (0.01)	40.57 (0.04)	0.15 (0.01)	0.02 (0.01)	99.57 (0.05)	38	23.59 (1.09)	10.52 (0.35)	498.5 (15.49)	BDL < 0.301	0 (0)	15
E7.2_II_SB_A	39.04 (0.05)	19.89 (0.15)	0.45 (0.01)	40.61 (0.09)	0.14 (0.01)	BDL < 110	100.31 (0.17)	19	28.33 (1.48)	22.42 (0.72)	496.3 (18.67)	BDL < 0.38	0 (0)	20

588 Table 5 (continued).

Sample	[a]SiO$_2$ wt.%	[a]FeO wt.%	[a]MnO wt.%	[a]MgO wt.%	[a]CaO wt.%	[a]Na$_2$O wt.%	[a]Total wt.%	[a]n	[b]Sc µg/g	[b]V µg/g	[b]Ni µg/g	[b]Cs µg/g	[b]U µg/g	[b]n
E7.2_II_SB_B	39.11 (0.05)	19.58 (0.14)	0.64 (0.01)	40.86 (0.13)	0.16 (0.01)	BDL < 109	100.52 (0.08)	12	26.65 (1.98)	17.84 (0.75)	187.2 (13.49)	BDL < 0.569	0 (0)	7
E4.3_H2_A	38.56 (0.02)	21.58 (0.05)	0.6 (0.01)	38.4 (0.03)	0.10 (0.01)	0.02 (0.01)	99.47 (0.06)	44	25.9 (1.86)	6.05 (0.59)	523.3 (29.09)	BDL < 0.563	0 (0)	6
E2.3_II_H2_A	37.75 (0.02)	26.06 (0.06)	0.51 (0.01)	34.43 (0.04)	0.14 (0.01)	0.02 (0.01)	99.1 (0.05)	32	19.9 (1.37)	11.53 (0.58)	277.7 (16.99)	BDL < 0.269	0 (0)	11
E2.3_II_H2_B	37.79 (0.04)	25.92 (0.06)	0.46 (0.01)	34.43 (0.05)	0.14 (0.01)	0.02 (0.01)	98.98 (0.06)	24	24.28 (1.18)	10.56 (0.43)	463.2 (16.32)	BDL < 0.251	0 (0)	15
E7.3_SB_A	37.24 (0.05)	26.91 (0.11)	0.56 (0.01)	34.19 (0.1)	0.12 (0.01)	0.02 (0.01)	99.25 (0.08)	21	70.1 (4.8)	35.11 (2.24)	180 (39.29)	BDL < 0.848	0 (0)	2

589 See Table 4 for definitions of "n," uncertainty reporting, detection limits, and rounding conventions.

590 [a]EPMA analysis.

591 [c]LA-ICP-MS analysis. Cs and U included to illustrate their incompatibility in olivine and suitability as proxy elements for distinguishing
592 olivine from the glass matrix.

593

594 **4.4. Partitioning of redox-sensitive elements between olivine and melt**

595   This section explores partitioning behavior of hetero-valent elements between olivine

596 and silicate melt and their potential to be used as redox sensors in the relevant arc magmatic

597 fO_2 range. Element contents were normalized to those of monovalent elements with the same

598 charge and similar ionic radius to derive exchange coefficients that are less sensitive to

599 temperature and compositional variations in melt and olivine.

600 *4.4.1. Exploration of potential redox-sensitive element partitioning*

601   To explore the dataset, we applied a combined PCA and CorMat approach using the

602 following inputs: 1) major element compositions of olivine, glass, and starting material;

603 2) intensive parameters (P, T, and fO_2); 3) modeled (MELTS, H_2O_{mod}), and measured H_2O

604 contents; and 4) silicate melt properties such as ASI (aluminum saturation index, in mol) and

605 NBO/T. NBO/T was calculated following Eq. (3) from Zajacz and Tsay (2019), which is based

606 on the formulation of Mysen and Richet (2005).

607   A second CorMat was generated using a reduced dataset that included partition

608 coefficients ($D_{[i]}^{[Ol/melt]}$) for compatible elements (*i*) in olivine with special focus on redox-

609 sensitive indicators: $D_{[V]}^{[Ol/melt]}$, $D_{[Fe]}^{[Ol/melt]}$, Fe-Mg exchange coefficient ($K_{D[Fe_T/Mg]}^{[Ol/melt]}$, defined as the

610 molar Fe_T/Mg-ratio, where Fe_T is derived from total FeO-content of both olivine and silicate

611 glass), and V-Sc exchange coefficient ($K_{D[V/Sc]}^{[Ol/melt]}$). For further details see Table S.13, S14 and

612 Figure S.12 in the supplementary material. $D_{[V]}^{[Ol/melt]}$ and $K_{D[V/Sc]}^{[Ol/melt]}$ showed the strongest

613 negative correlation with changing fO_2, followed by $D_{[Fe]}^{[Ol/melt]}$ and $K_{D[Fe_T/Mg]}^{[Ol/melt]}$ with moderate to

614 strong correlation, which are consistent with their known redox sensitivity (Osborn, 1959;

615 Carmichael and Ghiorso, 1990; Ehlers et al., 1992; Mysen, 2006; Blundy et al., 2020;

616 Burnham et al., 2020; Leuthold et al., 2023). $D_{[i]}^{[Ol/melt]}$ values for other heterovalent elements

617 demonstrated weak or non-significant correlations within the studied fO_2 range. Based on

618 these findings, the three relevant redox-sensitive systems (V, V-Sc, and Fe-Mg) are

619 discussed in order of decreasing significance in the following subsections.

620   *4.4.2. V-based oxybarometry between olivine and melt*

621   Among all elements analyzed, V demonstrates the strongest correlation with fO_2. Fig.

622   5 compares $D_{[V]}^{[Ol/melt]}$ with $K_{D[V/Sc]}^{[Ol/melt]}$ as well as the partitioning of Sc ($D_{[Sc]}^{[Ol/melt]}$) and V-content in

623   the glass and olivine as a function of fO_2. Although the $\log(D_{[Sc]}^{[Ol/melt]})$ ranges from -0.624 to

624   0.453, it demonstrates no apparent dependence on fO_2 and it appears instead to be

625   influenced by NBO/T and temperature (Fig. 5c). The V distribution in both glass and olivine

626   (subsection 4.3.2) shows a more pronounced systematic variation with fO_2 (Fig. 5d). While

627   the $\log(D_{[V]}^{[Ol/melt]})$ varies from -0.359 to -2.232, $\log(K_{D[V/Sc]}^{[Ol/melt]})$ shows values from -0.681 to -

628   1.844, both with increasing fO_2 (Fig. 5a and b). The $K_{D[V/Sc]}^{[Ol/melt]}$ is less affected by increasing

629   NBO/T with decreasing temperature, hence increasing fractional crystallization. Linear

630   regression fits for the two starting materials (MKCA vs. SHOSH) show no significant

631   difference, as their 95 % confidence intervals largely overlap across the studied fO_2 range.

632   The strong negative correlations for both $D_{[V]}^{[Ol/melt]}$ and $K_{D[V/Sc]}^{[Ol/melt]}$ with logfO_2 (ΔFMQ) can be

633   expressed by the following linear regressions including ±1SE, whereas the outlier

634   E7.3_SB_A was excluded from the fitting process for equation Eq. (3):

635    $$\Delta FMQ = (\log(D_V^{[Ol/melt]}))_{(y)} + 1.30027_{(t)}^* \pm 0.02464_{(\Delta t)}^*) / -0.2214_{(m)} \pm 0.01307_{(\Delta m)} \quad (3)$$

636    $$\Delta FMQ = (\log(K_{D[V/Sc]}^{[Ol/melt]}))_{(y)} + 0.98079_{(t)} \pm 0.02244_{(\Delta t)}) / -0.20567_{(m)} \pm 0.01231_{(\Delta m)} \quad (4)$$

637   In the special case for Eq. (3) the intercept* was fixed for the fitting process. Both its value

638   and corresponding fitting error are derived from an exploratory fitting process by using

639    $D_{[V]}^{[Ol/melt]}$ instead of $\log(D_{[V]}^{[Ol/melt]})$ (see Figure S.13). Equations (3) and (4) calculate logfO_2

640   (ΔFMQ) generally within a 2σ propagated median uncertainty (cf. Eq. (1)) of 0.38 and

641   0.44 log units, respectively. Note that the propagated analytical uncertainty of both the

642   partition and exchange coefficient is included. Regarding the calibration dataset (n = 32)

643   they show within 0.5 ΔFMQ threshold value a success rate of reproducibility of 84.4% and

644   90.6%, respectively.

645 *4.4.3. Fe-Mg exchange coefficient between olivine and melt*

646   The $\log(\mathrm{K}_{\mathrm{D[Fe_T/Mg]}}^{\mathrm{[Ol/melt]}})$ demonstrates potential as an oxybarometer at redox conditions

647 above ~FMQ -0.5 as it follows a well-defined sigmoidal trend with changing $f\mathrm{O_2}$ (Fig. 6).

648 While melt composition (MKCA vs. SOSH) displays no significant effect on it, as the 95 %

649 confidence intervals overlap (Fig. 6a), the $\log(\mathrm{K}_{\mathrm{D[Fe_T/Mg]}}^{\mathrm{[Ol/melt]}})$ seems to be influenced by

650 temperature and melt polymerization (NBO/T), alongside $f\mathrm{O_2}$ (Fig. 6a and b). This effect

651 appears to be stronger with decreasing $f\mathrm{O_2}$, as reflected by a sharp increase in the fayalite

652 component of olivine (expressed as molar fraction of fayalite, X_{Fay}, Fig. 6c), which also

653 captures the influence of temperature (Fig. 6a). To better understand the behavior of the

654 $\log(\mathrm{K}_{\mathrm{D[Fe_T/Mg]}}^{\mathrm{[Ol/melt]}})$, we model it as a function of $f\mathrm{O_2}$, incorporating the variability from NBO/T and

655 X_{Fay}:

$$
\begin{aligned}
\log(K_{D[Fe_T/Mg]}^{[Ol/melt]})_{\mathrm{mod}} &= -0.4523 - 0.0253*\Delta FMQ - 0.0116*\Delta FMQ^2 \\
&\quad + 0.0009*\Delta FMQ^3 - 0.1593*(1+3*C)*3*NBO/T
\end{aligned}
$$

$$\text{with } C:$$

656   (5)

$$
\begin{aligned}
&\text{for } X_{Fay}(mol) > 0.225:\ C = X_{Fay}(mol) - 0.225 \\
&\text{for } X_{Fay}(mol) \le 0.225:\ C = 0
\end{aligned}
$$

657 The modelled Fe-Mg exchange coefficient ($\log(\mathrm{K}_{\mathrm{D[Fe_T/Mg]}}^{\mathrm{[Ol/melt]}})_{\mathrm{mod}}$) as a function of $f\mathrm{O_2}$ is illustrated

658 by Fig. 6b. A polynomial regression model comparing $\log(\mathrm{K}_{\mathrm{D[Fe_T/Mg]}}^{\mathrm{[Ol/melt]}})$ and $\log(\mathrm{K}_{\mathrm{D[Fe_T/Mg]}}^{\mathrm{[Ol/melt]}})_{\mathrm{mod}}$ yields

659 a correction equation, providing a compositionally adjusted Fe-Mg exchange coefficient (

660 $\log(\mathrm{K}_{\mathrm{D[Fe_T/Mg]}}^{\mathrm{[Ol/melt]}})_{cor}$) that accounts for the NBO/T and X_{Fay} effects:

$$
\begin{aligned}
\log(K_{D[Fe_T/Mg]}^{[Ol/melt]})_{cor} &= 1.0868*\log(K_{D[Fe_T/Mg]}^{[Ol/melt]})_{measured} + 0.0517*NBO/T \\
&\quad -1.1534*X_{Fay} - 2.287*\log(K_{D[Fe_T/Mg]}^{[Ol/melt]})_{measured}*X_{Fay}
\end{aligned}
$$

661   (6)

662 A sigmoidal regression fit of the $\log(\mathrm{K}_{\mathrm{D[Fe_T/Mg]}}^{\mathrm{[Ol/melt]}})_{cor}$ versus $f\mathrm{O_2}$ relationship defines an

663 oxybarometer. The resulting equation (including ±1SE uncertainty on the fitting parameters)

664 is defined with fixed lower and upper asymptotes at -2.2 (estimated by experimental data at

665   very oxidizing conditions, see Figure S. 14) and -0.48 (derived from the canonical value of

666   0.3+0.03 uncertainty after Roeder and Emslie, 1970), respectively, as follows:

667

$$\Delta FMQ = LOGx0 - \left(\log_{10} \left[1.51851 \Big/ (y+2.2) \right] - 1 \right) \Big/ p \ (7)$$

668   with LOGx0 = 8.08156±0.28604, p = -0.18550±0.00927 and y = $\log(K_{D[Fe_T/Mg]}^{[Ol/melt]})_{cor}$. For more

669   details about the generation of equations Eq. (5) and (6), see supplementary material S4

670   and Table S.15. Equation (7) calculates log$f$O$_2$ (ΔFMQ) generally within a 2σ propagated

671   median uncertainty of 0.92 log units. Applying Eq. (7) on the calibrated dataset shows a

672   success rate of reproducibility of 94% within the 0.5 ΔFMQ threshold. To calculate the

673   propagated uncertainty, apply Eq. (2) with uncertainty values provided under Eq. (7).

674   ## 5. Discussion

675   This chapter evaluates the performance of the applied oxybarometric systems and

676   compares them with previous studies. A detailed discussion on the quality of the

677   experimental approach is provided in the supplementary material (S3-quality of

678   experiments). Further details on fitting statistics are available in supplementary material

679   (Table S.16).

680   ### 5.1. Sensitivity and robustness of geochemical oxybarometers

681   The previous chapter demonstrated the improved robustness of the V/Sc

682   oxybarometer, which will now be contextualized alongside other oxybarometric systems.

683   Vanadium-, V-Sc-, and Fe-Mg-based oxybarometers will be discussed in order of increasing

684   complexity, with comparisons to prior experimental studies.

685   *5.1.1. V oxybarometry*

686   Fig. 8a compares the new data reported in this study with existing experimental data.

687   Over a broad fO$_2$ range, the distribution of $\log(D_{[V]}^{[Ol/melt]})$ as a function of fO$_2$ is sigmoidal. The

688   most experimental data falls within the fO$_2$ range FMQ -5 to +5. The values for $\log(D_{[V]}^{[Ol/melt]})$

689   of this study are within the range of those reported by previous studies except for a single

690　　outlier (E7.3_SB_A), previously noted in subsection 4.4.2. To evaluate the potential causes,

691　　we examine several parameters.

692　　　　For example, this outlier could reflect a failure of fO_2 control, leading to redox

693　　disequilibrium. However, no Fe-Mg zoning was observed in olivine from experiment

694　　E7.3_SB_A, as confirmed by low standard errors in FeO measurements. In addition, fO_2

695　　control was ensured by confirmed water saturation and the presence of Co and CoO_2 in the

696　　surrounding solid buffer (Table 3).

697　　　　Another possibility for this shift would be an analytical artifact. LA-ICP-MS

698　　measurements on small experimentally grown olivine crystals can demonstrate difficulties

699　　due to contamination by other phases (i.e., glass matrix). If this was the case for experiment

700　　E7.3_SB_A, slight glass or spinel contaminations would be easily identified by the presence

701　　of incompatible elements in olivine (such as U) or elements characteristic of spinel (i.e., Cr).

702　　But both analytical artefacts can be ruled out (Table 5).

703　　　　We infer that the degree of polymerization accounts for the outlier observed in this

704　　study. Specifically, NBO/T decreases sharply to 0.212, representing a drop of 0.173 relative

705　　to the previous step at 960 °C (where NBO/T was 0.385). In contrast, earlier temperature

706　　steps showed much smaller changes (ΔNBO/T ≤ 0.105). This decrease coincides with a

707　　pronounced reduction in V-concentration in the glass matrix to 80.3 µg/g, compared to the

708　　median value of 250.8±36.7 µg/g observed in all other experiments (Fig. 5d).

709　　Simultaneously, the corresponding olivine shows a nearly twofold increase in V-

710　　concentration (35.1 µg/g), relative to olivines from other experiments at the same fO_2 but

711　　different temperatures (V: 13.3-22.4 µg/g; T = 1019-960 °C; Table 5). This coincides with

712　　drastic increases in $\log(D^{[Ol/melt]}_{[Sc]})$ as illustrated by Fig. 5c. In fact, previous studies

713　　incorporated NBO/T as a linear factor in their V oxybarometers (Wang et al., 2019; Erdmann

714　　et al., 2024). While NBO/T will be influenced by fO_2 (i.e., through changes in the Fe^{2+}/Fe^{3+}

715　　ratio in the silicate melt and consequently melt-polymerization) no systematic effect on the

716　　$D^{[Ol/melt]}_{[V]}$ is observed in this study.

717   We conclude that the observed outlier in $D_{[V]}^{[Ol/melt]}$ rises only under conditions of a

718   pronounced change in melt polymerization, which kinetically influences the diffusion of trace

719   elements between olivine and silicate melt (Ni et al., 2015). This is likely driven by

720   substantial undercooling (i.e., a large temperature difference between the liquidus and the

721   experimental run temperature). This agrees with the experimentally observed increase in

722   relative undercooling. After the first temperature step (T = 1019 °C), the liquidus of the

723   residual melt is experimentally constrained, so subsequent undercooling largely reflects the

724   imposed temperature decrement. However, because the residual melt becomes increasingly

725   evolved and viscous, even a slightly larger decrement (40 °C between 960 °C and 920 °C

726   vs. ~30 °C in earlier steps) leads to a greater relative undercooling, enhancing kinetic effects

727   such as diffusion-limited trace-element partitioning.

728   Given this outlier and to ensure robust sigmoidal regression fitting, we applied a

729   filtering approach designed to minimize the influence of outliers while preserving asymptotic

730   behavior. The resulting dataset (n = 167) was derived from the original 344 experiments, as

731   detailed in Table S.17 of the supplementary material. This approach ensures that only

732   extreme outliers are removed, affecting mostly the two endmembers of the sigmoidal curve.

733   The resulting subset of 167 experiments was used for model calibration, while the remaining

734   data serve as an independent test set for validation. Fig. 8b provides a closer view of the

735   fO_2 window relevant for terrestrial systems. A linear fit is compared to the previously applied

736   sigmoidal model. While both show similar predictive accuracy for fO_2 up to FMQ +3, the

737   linear model offers theoretically lower parameter uncertainty and is simpler to implement,

738   which can enhance its robustness and practical utility when used for estimating redox

739   conditions in this range. The linear fit from Eq. (3) of this study, closely aligns with the other

740   two regression fits. While our results for $\log(D_{[V]}^{[Ol/melt]})$ versus fO_2 align well with previous

741   research (Canil and Fedortchouk, 2001; Mallmann and O'Neill, 2013; Shishkina et al., 2018;

742   Wang et al., 2019; Erdmann et al., 2024) applying our fitted models offer a twofold

743   advancement: 1) a universal oxybarometer applicable across a broad fO_2 range; and 2) an

744   optimized version with significantly lower prediction uncertainties tailored for hydrous melts

745 within the relevant $f\mathrm{O}_2$ window. In the following paragraph, we discuss potential sources of

746 variance in the complete dataset to substantiate the initial data filtering approach.

747   The most likely reason for the variance of the data set is the influence of intensive or

748 extensive parameters such as pressure, temperature and melt composition on $\mathrm{D}_{[\mathrm{V}]}^{[\mathrm{Ol/melt}]}$.

749 Mallmann and O'Neill (2009) observed a noticeable influence of both melt and olivine

750 composition on the $\mathrm{D}_{[\mathrm{V}]}^{[\mathrm{Ol/melt}]}$; however, Mallmann and O'Neill (2013) concluded that this effect

751 is minimal. Regarding the effect of temperature, previous studies present conflicting

752 conclusions: some demonstrate temperature dependence of $\mathrm{D}_{[\mathrm{V}]}^{[\mathrm{Ol/melt}]}$ (Mallmann and O'Neill,

753 2013; Laubier et al., 2014; Wang et al., 2019; Erdmann et al., 2024) while others propose

754 the absence or negligibility of such a relationship (Canil, 1997, 1999; Canil and Fedortchouk,

755 2001; Leuthold et al., 2023). Given the compositional variability of olivine and silicate melt

756 and the wide $f\mathrm{O}_2$-temperature range represented in Fig. 8a, the spread of the main dataset

757 cannot be explained by composition or temperature alone. This variability contributes to the

758 ~1 log unit uncertainty in $\Delta\log f\mathrm{O}_2$ prediction, as shown in Fig. 8b. A CorMat conducted on

759 the experimental dataset (including this study) revealed no systematic shift in predicted

760 $\Delta\log f\mathrm{O}_2$ as a function of temperature (see Table S.18).

761   Another factor could be the composition of the starting material, including its V-

762 content. This study demonstrates that the studied melt compositional variance

763 encompassing a large fraction of arc magmas does not yield a statistically significant effect

764 on $\mathrm{D}_{[\mathrm{V}]}^{[\mathrm{Ol/melt}]}$ (Fig. 5). In addition, Laubier et al. (2014) report that the V-content in the starting

765 material does not influence the final V partition coefficient between olivine and silicate melt.

766 Although most experiments are conducted under ambient pressure and anhydrous

767 conditions, it was proposed that V partitioning is unaffected by H_2O (Shishkina et al., 2018)

768 and that the influence of pressure is negligible (Canil, 1997; Canil and Fedortchouk, 2001;

769 Mallmann and O'Neill, 2013; Wang et al., 2019).

770   An experimental artifact could also be considered as a potential explanation. Erdmann

771 et al. (2024) outline the challenges of achieving precise and accurate redox conditions

772 depending on the experimental apparatus being applied (i.e., piston cylinder). Earlier,

773 Mallmann and O'Neill (2009) noted that an observed temperature influence on V partition

774 coefficient in case of garnet- and clinopyroxene melt pairs might result from fO_2

775 overestimation when using a ReReO$_2$ solid buffer. This could be explained by a detectable

776 high standard deviation on the V partition and/or Fe-Mg exchange coefficient as a

777 consequence of redox disequilibrium. While some variance in the dataset may arise from

778 redox disequilibrium, as suggested by core-to-rim Fe-Mg zoning in an outlier experiment

779 from Dygert et al. (2020), such effects are not evident in the majority of published

780 experiments. Alternatively, these outliers and deviations may reflect incomplete attainment

781 of kinetic equilibrium as discussed for experiment E7.3_SB_A.

782 Overall, using $D_{[V]}^{[Ol/melt]}$ as oxybarometer (V oxybarometer) is a powerful tool to track

783 magmatic redox conditions. A sigmoidal regression line can be fitted to all experimental data

784 based on the theoretical explanation of the behavior of the bulk V partitioning with changing

785 fO_2 (Mallmann et al., 2022). The corresponding equation, where logfO_2 is expressed relative

786 to ΔFMQ, is defined as follows:

787
$$\Delta FMQ = LOGx0 - \left(\log_{10}\left[4.34642 \middle/ (y + 3.11912) \right] - 1 \right) \middle/ p \quad (8)$$

788 with LOGx0 = -1.72333±0.0473, p = -0.09895±0.00175 and y = $D_{[V]}^{[Ol/melt]}$.

789 Eq. (8) demonstrates a 2σ propagated median uncertainty of 0.32 log units over the

790 fO_2 range from ΔFMQ -5 to +5, which highly depends on the precise determination of the

791 $D_{[V]}^{[Ol/melt]}$ and increases towards extreme fO_2 endmembers. Applying (8) on the calibrated

792 dataset shows a success rate of reproducibility of 83% within 0.5 ΔFMQ threshold value. If

793 the fO_2 range is limited to FMQ -5 to +3.5, a linear fitting expression can be applied as

794 follows:

795
$$\Delta FMQ = (\log(D_V^{[Ol/melt]}) + 1.34021 \pm 0.01144) / -0.23336 \pm 0.00405 \quad (9)$$

796   Eq. (9) demonstrates a 2σ propagated median uncertainty of 0.34 log units over the

797   calibrated fO_2 range. It reproduces fO_2 better (88.6%) than Eq. (8) but only within the

798   calibration range. Beyond that the linear fit leads to significant overestimation of fO_2. Note

799   that Eq. (9) shows values for the fitting parameters similar to Eq. (3).

800   *5.1.2. V-Sc oxybarometry*

801   Although the V oxybarometer is well-suited to track fO_2 in magmatic systems, the

802   previous subsection highlighted its potential sensitivity to kinetic effects. Therefore, the

803   V oxybarometer can be improved in terms of its robustness by coupling it with the chemically

804   similar but redox-independent Sc as demonstrated in Fig. 5b.

805   Comparing the V-Sc exchange coefficient between various experimental studies and

806   with the V partition coefficient for olivine-melt pairs reveals three key differences across a

807   broad range of fO_2: 1) The number of extreme outliers is removed (i.e., this study); 2) The

808   offset between the trend defined by our data and those from previous studies can be

809   attributed to differences in silicate melt NBO/T (Fig. 9a); and 3) enhanced variance of $D_{[Sc]}^{[Ol/melt]}$

810   for anhydrous experiments (Fig. 9b). Given the strong agreement between V-partitioning

811   data from this and previous studies (Fig. 8) the observed offset in Fig. 9a must be linked to

812   the olivine/melt partitioning of Sc. Fig. 9b highlights the non-linear increase of $\log(D_{[Sc]}^{[Ol/melt]})$

813   with decreasing temperature, whereas the V partition coefficient remains independent from

814   temperature (Figure S.15). The variability in V partitioning is instead primarily controlled by

815   fO_2. As silicate melt composition (e.g., NBO/T) and temperature are correlated variables in

816   this study, it cannot be defined just based on our data which variable affects $D_{[Sc]}^{[Ol/melt]}$ more.

817   However, statistical testing pointed out that NBO/T is a strong mediator between temperature

818   and $D_{[Sc]}^{[Ol/melt]}$ (Figure S.16, and Tables S.14 and S.18).

819   Mallmann and O'Neill (2013) observed a correlation between $D_{[Sc]}^{[Ol/melt]}$ and temperature,

820   which formed the basis of their proposed Sc-Y geothermometer. However, Mallmann and

821   O'Neill (2013) also pointed out a noticeable effect of both melt and olivine compositions on

822    $D_{[Sc]}^{[Ol/melt]}$. A clear correlation between NBO/T and $\log(D_{[Sc]}^{[Ol/melt]})$ might be masked by the higher

823   variability of $D_{[Sc]}^{[Ol/melt]}$ in anhydrous experiments (Fig. 9b). Kelley and Cottrell (2012) address

824   the limitation of the V/Sc proxy, noting that its calibration under anhydrous, atmospheric

825   conditions may not be applicable to the high-pressure, hydrous environments of mantle

826   wedge melting. Another possibility could be an analytical artefact for not accounting the

827   isobaric interference of the $^{29}Si^{16}O$ signal to ^{45}Sc (subsection 3.3.1, in this study only about

828   1 µg/g). Although this has been corrected for in the present study and in some previous

829   works (Mallmann and O'Neill, 2009, 2013), such interference would in a large part be

830   canceled out during the calculation of the partition coefficient between olivine and silicate

831   melt (Mallmann and O'Neill, 2013). This suggests that the parallel offset observed in Fig.

832   9a, reflects the complex behavior of $D_{[Sc]}^{[Ol/melt]}$ in response to changes in degree of melt

833   polymerization, as illustrated in Fig. 9b. Temperature, melt composition (i.e., NBO/T), and

834   water content all contribute to this behavior, highlighting their combined influence on

835   diffusivity of Sc.

836   However, this study demonstrates that the V-Sc oxybarometer outperforms models

837   based solely on V partitioning between olivine and silicate melt. Given the high-precision

838   analysis of V and Sc in our setup, we recommend applying our V-Sc oxybarometer (Eq. (4))

839   for hydrous arc magmatic systems with NBO/T ≤ 0.6 which falls within the observed range

840   for andesitic to basaltic rocks (Mysen et al., 1982).

841   *5.1.3. Fe-Mg-based oxybarometry*

842   Subsection 4.4.3. demonstrated that the $\log(K_{D[Fe_T/Mg]}^{[Ol/melt]})$ correlates with fO_2 and the

843   corresponding equation Eq. (7) can be used as a Fe-Mg-oxybarometer within the calibrated

844   range of this study. The Fe^{2+}-Mg exchange coefficient ($K_{D[Fe/Mg]}^{[Ol/melt]}$) between olivine and silicate

845   melt is known to be relatively insensitive to pressure, temperature and melt composition

846   (Roeder and Emslie, 1970; Ford et al., 1983; Ulmer, 1989; Matzen et al., 2011; Blundy et

847   al., 2020; Saper et al., 2022). Blundy et al. (2020) and references therein outlined the weak

848   to negligible effect of pressure, temperature, composition and H_2O content on $K_{D[Fe/Mg]}^{[Ol/melt]}$.

849   Despite the fact that Fe is incorporated in olivine only as ferrous iron, only a few studies

850   considered the use of $K_{D[Fe_T/Mg]}^{[Ol/melt]}$ as oxybarometer (Roeder and Emslie, 1970; Blundy et al.,

851   2020; Matzen et al., 2022).

852   Based on $K_{D[Fe/Mg]}^{[Ol/melt]}$, the measured olivine composition and MgO content in the silicate

853   melt, we estimated the concentration of Fe(II)O in the melt, which in turn was used to

854   calculate the Fe^{3+}/Fe_{tot} ratios in the melt by comparing it to the measured FeO_{tot} value. The

855   values of $K_{D[Fe/Mg]}^{[Ol/melt]}$ were calculated by using the method of Toplis (2005) and Blundy et al.

856   (2020). Fig. 10 compares the such estimated Fe^{3+}/Fe_{tot} ratios in the silicate melt with the

857   prediction of various models (Kress and Carmichael, 1991; Jayasuriya et al., 2004; Putirka,

858   2016; Borisov et al., 2018).

859   A key observation is that the experimental dataset defines a trend parallel with the

860   model predictions. However, the calculated values fall significantly below the predicted

861   curves. Indeed, at our lowest experimental fO_2, negative Fe^{2+}/Fe_{tot} ratios are predicted (Fig.

862   10). As equilibrium has been demonstrated for our experiments, the only possible

863   explanation for the negative values is that the model-calculated $K_{D[Fe/Mg]}^{[Ol/melt]}$ values are

864   underestimated. Such underestimation would yield a systematic shift of our dataset to lower

865   Fe^{2+}/Fe^{3+} independently of fO_2, which is consistent with the observation in Fig. 10. Indeed,

866   if we increased the value of $K_{D[Fe/Mg]}^{[Ol/melt]}$ by ~25 rel.% the calculated Fe^{2+}/Fe_{tot} ratios are

867   consistent with the model predictions. Such an offset is plausible as the calibration dataset

868   of Toplis (2005) and Blundy et al. (2020) is dominated by data from experiments conducted

869   at significantly higher temperature ($T \geq 1025$ C) and with predominantly more mafic melt

870   compositions. In fact, Blundy et al. (2020) addressed limitations in their calibrations,

871   particularly for melts with ~60 wt.% SiO_2.

872   Overall, we conclude that the $\log(K_{D[Fe_T/Mg]}^{[Ol/melt]})$ can serve as an oxybarometer (for

873    $fO_2 >$ ~FMQ -0.5) in experimental studies, providing reliable fO_2 estimates under controlled

874 conditions. When the composition of the silicate melt in equilibrium with the olivine can be

875 determined, it may also be useful for field-based research, where a rapid shift in redox

876 conditions may be effectively recorded by diffusive Fe-Mg exchange between olivine and

877 silicate melt (Shea et al., 2023). In contrast, V-based oxybarometers, which are less affected

878 by diffusion, preserve the original magmatic fO_2 recorded by melt inclusions (Canil, 1997,

879 2002; Anser Li and Aeolus Lee, 2004). Thus, combining these approaches offers

880 complementary insights into both the initial and evolving redox conditions in natural

881 magmatic systems.

5.2. Comparison of oxybarometers

883 To evaluate the performance of V-based oxybarometers under experimental

884 conditions, Fig. 11 uses the dataset from subsection 4.4.2 to compare calculated fO_2 values

885 with those determined experimentally. This comparison covers a large proportion of that

886 being relevant for terrestrial systems (Mallmann et al., 2022). For a quantitative comparison

887 of accuracy and precision of each oxybarometer, Fig. 12 demonstrates the corresponding

888 concordance correlation coefficients (CCC, Fig. 12a), 2σ propagated uncertainty (Unc., Fig.

889 12b) and root mean square error (RMSE, Fig. 12c). Since the oxybarometers of this study

890 are calibrated using the entire dataset of this study such a high CCC-value is expected. To

891 strengthen the evaluation, we included a comparison of the best-performing oxybarometers

892 from this study using an extended dataset, alongside the top-performing model from previous

893 studies. This allows the evaluation of potential overfitting and provides a robust test for the

894 practical applicability of the oxybarometer.

895 All oxybarometers of this study show very good performance (CCC > 0.9) accompanied by

896 low RMSE values. The Fe-Mg-oxybarometer (Eq. (7)) demonstrates the highest uncertainty

897 (2σ, ~1 ΔFMQ), while V-Sc oxybarometer performs at best regarding all parameters

898 combined (CCC = 0.93, RMSE = 0.252, 2σ-Unc. ~0.41 ΔFMQ). The oxybarometers of

899 Erdmann et al. (2024) and Shishkina et al. (2018) are comparable in their performance with

900 CCC around 0.85. Only the oxybarometers of Wang et al. (2019) and Mallmann and O'Neill

901 (2013) display a similar systematic overestimation of the measured fO_2 (Fig. 11).

902   Consequently, both reveal lower CCC values (CCC < 0.6), higher RMSE and propagated

903   uncertainties (2σ, > 1 ΔFMQ). The first published oxybarometer by Canil and Fedortchouk

904   (2001) shows an almost equally good performance as oxybarometers of this study. As the

905   V-Sc oxybarometer (Eq. (2)) is only calibrated within the constraints of this study, we

906   compare the most promising V oxybarometers of this study (Eqs. (8) and (3)) with the one

907   from Canil and Fedortchouk (2001) on an extended dataset (n = 345). All three show

908   elevated RMSE compared to their application on the small dataset (n = 31, this study) but

909   comparable CCC and propagated uncertainty values. V oxybarometer of Eq. (8)

910   demonstrates the best performance (CCC > 0.9 and 2σ-Unc. ~0.5 ΔFMQ). It reflects its

911   advantage to be more precise and accurate for very oxidizing conditions (> FMQ +3.5),

912   where a linear regression fits to systematic overestimation of fO_2.

913   Overall, the V-based oxybarometers of this study offering low calibration uncertainties

914   (2σ-Unc. < 0.5 ΔFMQ), high precision and accuracy along with flexibility and robustness

915   across a wide *P-T-X-f*O_2 space. Nevertheless, the V-Sc oxybarometer displays the best

916   performance (i.e., robustness) within the calibration range (NBO/T ≤ 0.6) of this study and

917   offers a high precision oxybarometer for olivine-bearing hydrous basaltic-andesitic magmatic

918   systems, typically found at convergent plate boundaries.

6. Implications

920   As olivine is a common phenocryst in hydrous basaltic to andesitic magmas in volcanic

921   arcs, the oxybarometers proposed in this study will facilitate improved reconstruction of the

922   redox evolution of arc magmatic systems. They will allow to reconstruct the initial fO_2 of

923   primitive magmas and potential redox changes during early stages of magma differentiation

924   with high precision and accuracy (2σ < 0.4 ΔFMQ) independent of melt composition. This, in

925   turn, will enhance our understanding of magma genesis, the role of fO_2 in controlling volatile

926   speciation, metal transport capacity, and its influence on volcanic degassing.

927   We recommend the following procedure to apply $D_{[V]}^{[Ol/melt]}$ and $K_{D[V/Sc]}^{[Ol/melt]}$ as

928   oxybarometers to enhance accuracy and precision:

43

929　　　(1) Initial calculation: Use Eq. (8) $\left[fO_2(\Delta FMQ) = f_{sig}\left(\log(D_V^{[Ol/melt]}) \right) \right]$ to estimate the fO_2.

930　　　(2) Validation and cross-check: If the calculated fO_2 falls within a range of FMQ -5 to

931　　　　　FMQ +3.5, apply Eq. (3) $\left[fO_2(\Delta FMQ) = f_{lin}\left(\log(D_V^{[Ol/melt]}) \right) \right]$.

932　　　(3) If NBO/T ≤ 0.6 (NBO/T calculated following Eq. (3) from Zajacz and Tsay (2019),

933　　　　　which is based on the formulation of Mysen and Richet (2005)): Apply Eq. (4)

934　　　　　$\left[fO_2(\Delta FMQ) = f_{lin}\left(\log(K_{D[V/Sc]}^{[Ol/melt]}) \right) \right]$ to estimate the fO_2 with higher accuracy than in step

935　　　　　(1).

936　Importantly, better redox constraints also help assess the fertility of distinct magma series

937　such as calc-alkaline, shoshonitic, and even adakitic, which are associated with different

938　tectonic settings and ore deposit types (Sillitoe, 2010; Wilkinson, 2013; Richards, 2015;

939　Chen and Wu, 2020; Chiaradia, 2021; Heinrich, 2024). Future applications should focus on

940　silicate melt inclusions from both mineralized and barren systems to better constrain the

941　links between magma redox state, tectonic setting, and ore fertility of magmatic-

942　hydrothermal systems.

7. Conclusions

944　　　V partitioning between olivine and silicate melt serves as a reliable proxy for tracking

945　and quantifying redox changes in magmatic environments. This study bridges theoretical

946　understanding (i.e., Mallmann et al., 2022) and empirical calibration of V-based

947　oxybarometry in olivine silicate melt systems by integrating new complementary

948　experimental data with most available literature data by using statistical analysis. Through

949　precise and adaptable fO_2 control and refined LA-ICP-MS measurements on small olivine

950　crystals, this study extends our quantitative understanding of the fO_2 dependence of V and

951　Sc partitioning and Fe-Mg exchange between olivine and silicate melt to low-temperature

952　(T = 920-1019 °C) hydrous systems and tests the effect of silicate melt composition. We

953　have demonstrated the systematic independence of V partitioning between olivine and

954　silicate melt from intensive parameters (P-T-X and aH$_2$O). The remaining variance in V

955　partitioning reflects the precision and accuracy of experimental fO_2 control and may

956 additionally derive from potential analytical uncertainties and disruptions in the kinetic

957 equilibrium between olivine and silicate melt. The latter may be related to melt structure,

958 though the link to polymerization (e.g., NBO/T) remains tentative and may instead reflect

959 effects of undercooling in a few low-temperature experiments (T ~920 °C). Coupling the

960 $D_{[V]}^{[Ol/melt]}$ with redox-independent Sc partitioning compensates for this phenomenon improving

961 robustness and accuracy of reconstructing fO_2 but only within the calibrated range of this

962 study (i.e., NBO/T ≤ 0.6). Thus, we propose optimized V-based oxybarometers primarily in

963 the range of logfO_2 from FMQ -5 to FMQ +5 encompassing the relevant magmatic redox

964 conditions within the Earth system. The best of these is based on $D_{[V]}^{[Ol/melt]}$ and yields a

965 2σ uncertainty of < 0.33 log units on fO_2 estimation. Specifically, for magmatic arc systems

966 with fO_2 = FMQ -1 to FMQ +3.5, $K_{D[V/Sc]}^{[Ol/melt]}$ demonstrates a comparable 2σ uncertainty of

967 < 0.41 log units, and it shows enhanced robustness against kinetic effects if applied within

968 calibration range of this study (i.e., NBO/T ≤ 0.6). In addition, it will help gain new insights

969 into the role of magmatism and volcanic degassing in the redox evolution of the Earth's crust

970 and atmosphere.

Acknowledgments

CRediT authorship contribution statement

986 **Enzo-Enrico Cacciatore**: Writing – original draft, Visualization, Validation, Software,

987 Project administration, Methodology, Investigation, Formal analysis, Data curation,

988 Conceptualization. **Zoltán Zajacz**: Writing – review and editing, Validation, Supervision,

989 Project administration, Resources, Methodology, Funding acquisition, Conceptualization.

990 **Alexandra Tsay**: Methodology, Writing – review and editing and Resources. **Ivano**

991 **Gennaro**: Software. **Kalin Kouzmanov**: Methodology and Writing – review and editing.

992

Data availability

994 Data are available through Mendeley Data online at https://doi.org/10.17632/78jwj86xgd.1.

995

Appendix A. Supplementary material

997 The supplementary material includes the following: 1) S1_Supplementary_Tables, 2)

998 S2_Supplement_Quality_of_experimental_approach, 3) S3_Supplementary_Figures, and 4)

999 S4_Supplement_AI_generated_Python_Codes.

1000 S1: Excel tables with LA-ICP-MS, EPMA, and QEMSCAN analysis, as well as

1001 numerical data for statistical modeling (correlation matrix, fitting statistics, etc.) and

1002 coding input.

1003 S2: Details on the quality of experiments.

1004 S3: Figures illustrating precision and accuracy of EPMA and LA-ICP-MS

1005 measurements, along with statistical modeling.

1006 S4: AI-generated Python code.

1007 Supplementary material is available online at https://doi.org/10.17632/78jwj86xgd.1.

1008

1009

Declaration of Generative AI and AI-assisted technologies in the

1010

writing process

1011

During the preparation of this work, the authors used OpenAI's ChatGPT (Mar 14 version)

1012

to assist in generating Python code related to Equations Eq. (5), and (6). After using this

1013

tool, the authors reviewed and edited the content as needed and take full responsibility for

1014

the content of the publication.

1015

References

1016

Aeolous Lee, C.-T., Leeman, W.P., Canil, D., Li, Z.-X.A., 2005. Similar V/Sc Systematics in MORB and Arc Basalts: Implications for the Oxygen Fugacities of their Mantle Source Regions. Journal of Petrology 46(11), 2313-2336. https://doi.org/10.1093/petrology/egi056.

1017
1018
1019

Ai, Y., Chiaradia, M., Wu, C., Chen, H., 2024. Crustal magma oxidation state and endowments in porphyry copper deposits. Science China Earth Sciences. https://doi.org/10.1007/s11430-024-1429-6.

1020
1021
1022

Alex, A., Zajacz, Z., 2020. A new method to quantitatively control oxygen fugacity in externally heated pressure vessel experiments. European Journal of Mineralogy 32(1), 219-234. https://doi.org/10.5194/ejm-32-219-2020.

1023
1024
1025

Alex, A., Zajacz, Z., 2022. A new high-pressure experimental apparatus to study magmatic processes at precisely controlled redox conditions. American Mineralogist 107(4), 692-702. https://doi.org/10.2138/am-2022-7977.

1026
1027
1028

Anser Li, Z.-X., Aeolus Lee, C.-T., 2004. The constancy of upper mantle fO2 through time inferred from V/Sc ratios in basalts. Earth and Planetary Science Letters 228(3), 483-493. https://doi.org/10.1016/j.epsl.2004.10.006.

1029
1030
1031

Arató, R., Audétat, A., 2017. Experimental calibration of a new oxybarometer for silicic magmas based on vanadium partitioning between magnetite and silicate melt. Geochimica et Cosmochimica Acta 209, 284-295. https://doi.org/10.1016/j.gca.2017.04.020.

1032
1033
1034

Ballhaus, C., Berry, R.F., Green, D.H., 1991. High pressure experimental calibration of the olivine-orthopyroxene-spinel oxygen geobarometer: implications for the oxidation state of the upper mantle. Contributions to Mineralogy and Petrology 107(1), 27-40. https://doi.org/10.1007/BF00311183.

1035
1036
1037
1038

Blundy, J., Melekhova, E., Ziberna, L., Humphreys, M.C.S., Cerantola, V., Brooker, R.A., McCammon, C.A., Pichavant, M., Ulmer, P., 2020. Effect of redox on Fe−Mg−Mn exchange between olivine and melt and an oxybarometer for basalts. Contributions to Mineralogy and Petrology 175(11), 103-103. https://doi.org/10.1007/s00410-020-01736-7.

1039
1040
1041
1042

Borisov, A., Behrens, H., Holtz, F., 2018. Ferric/ferrous ratio in silicate melts: a new model for 1 atm data with special emphasis on the effects of melt composition. Contributions to Mineralogy and Petrology 173(12), 98-98. https://doi.org/10.1007/s00410-018-1524-8.

1043
1044
1045

Botcharnikov, R.E., Holtz, F., Behrens, H., 2015. Solubility and fluid−melt partitioning of H2O and Cl in andesitic magmas as a function of pressure between 50 and 500MPa. Chemical Geology 418, 117-131. https://doi.org/10.1016/j.chemgeo.2015.07.019.

Brounce, M., Kelley, K.A., Cottrell, E., Reagan, M.K., 2015. Temporal evolution of mantle wedge oxygen fugacity during subduction initiation. Geology 43(9), 775-778. https://doi.org/10.1130/G36742.1.

Bucholz, C.E., Kelemen, P.B., 2019. Oxygen fugacity at the base of the Talkeetna arc, Alaska. Contributions to Mineralogy and Petrology 174(10), 79-79. https://doi.org/10.1007/s00410-019-1609-z.

Burgisser, A., Scaillet, B., 2007. Redox evolution of a degassing magma rising to the surface. Nature 445(7124), 194-197. https://doi.org/10.1038/nature05509.

Burnham, A.D., Mallmann, G., Fonseca, R.O.C., 2020. Mineral-melt partitioning of redox-sensitive elements. Earth and Space Science Open Archive. https://doi.org/10.1002/essoar.10503118.1.

Canil, D., 1997. Vanadium partitioning and the oxidation state of Archaean komatiite magmas. Nature 389(6653), 842-845. https://doi.org/10.1038/39860.

Canil, D., 1999. Vanadium partitioning between orthopyroxene, spinel and silicate melt and the redox states of mantle source regions for primary magmas. Geochimica et Cosmochimica Acta 63(3), 557-572. https://doi.org/10.1016/S0016-7037(98)00287-7.

Canil, D., 2002. Vanadium in peridotites, mantle redox and tectonic environments: Archean to present. Earth and Planetary Science Letters 195(1), 75-90. https://doi.org/10.1016/S0012-821X(01)00582-9.

Canil, D., Fedortchouk, Y., 2001. Olivine-liquid partitioning of Vanadium and other trace elements, with applications to modern and ancient picrites. The Canadian Mineralogist 39(2), 319-330. https://doi.org/10.2113/gscanmin.39.2.319.

Carmichael, I.S.E., 1991. The redox states of basic and silicic magmas: a reflection of their source regions? Contributions to Mineralogy and Petrology 106(2), 129-141. https://doi.org/10.1007/BF00306429.

Carmichael, I.S.E., Ghiorso, M.S., 1990. The effect of oxygen fugacity on the redox state of natural liquids and their crystallizing phases. Reviews in Mineralogy and Geochemistry 24(1), 191-212. https://doi.org/10.1515/9781501508769-011.

Chen, H., Wu, C., 2020. Metallogenesis and major challenges of porphyry copper systems above subduction zones. Science China Earth Sciences 63(7), 899-918. https://doi.org/10.1007/s11430-019-9595-8.

Chiaradia, M., 2014. Copper enrichment in arc magmas controlled by overriding plate thickness. Nature Geoscience 7(1), 43-46. https://doi.org/10.1038/ngeo2028.

Chiaradia, M., 2021. Magmatic controls on metal endowments of porphyry Cu-Au deposits. In: Tectonomagmatic Influences on Metallogeny and Hydrothermal Ore Deposits: A Tribute to Jeremy P. Richards, Society of Economic Geologists. pp. 1-16. https://doi.org/10.5382/SP.24.01.

Churakov, S.V., Gottschalk, M., 2003. Perturbation theory based equation of state for polar molecular fluids: I. Pure fluids. Geochimica et Cosmochimica Acta 67(13), 2397-2414. https://doi.org/10.1016/S0016-7037(02)01347-9.

Cicconi, M.R., Moretti, R., Neuville, D.R., Guest, E., 2020. Redox Engine of Earth. Elements: An International Magazine of Mineralogy, Geochemistry, and Petrology 16(3), 148-220.

Cottrell, E., Birner, S., Brounce, M., Davis, F., Waters, L., Kelley, K., 2021. Oxygen Fugacity Across Tectonic Settings. Earth and Space Science Open Archive, 61-61. https://doi.org/10.1002/essoar.10502445.1.

da Silva, M.M., Holtz, F., Namur, O., 2017. Crystallization experiments in rhyolitic systems: The effect of temperature cycling and starting material on crystal size distribution. American Mineralogist 102(11), 2284-2294. https://doi.org/10.2138/am-2017-5981.

Dygert, N., Draper, D.S., Rapp, J.F., Lapen, T.J., Fagan, A.L., Neal, C.R., 2020. Experimental determinations of trace element partitioning between plagioclase, pigeonite, olivine, and lunar basaltic melts and an fO2 dependent model for plagioclase-melt Eu partitioning. Geochimica et Cosmochimica Acta 279, 258-280. https://doi.org/10.1016/j.gca.2020.03.037.

Earthchem Portal, 2021. EarthChem Database. https://www.earthchem.org/.

Ehlers, K., Grove, T.L., Sisson, T.W., Recca, S.I., Zervas, D.A., 1992. The effect of oxygen fugacity on the partitioning of nickel and cobalt between olivine, silicate melt, and metal. Geochimica et Cosmochimica Acta 56(10), 3733-3743. https://doi.org/10.1016/0016-7037(92)90166-G.

Erdmann, S., Pichavant, M., Gaillard, F., 2024. Mineral-melt vanadium oxybarometry for primitive arc magmas: effect of hydrous melt composition on fO2 estimates. Contributions to Mineralogy and Petrology 179(4), 39-39. https://doi.org/10.1007/s00410-024-02113-4.

Eugster, H.P., 1957. Heterogeneous reactions involving oxidation and reduction at high pressures and temperatures. The Journal of Chemical Physics 26(6), 1760-1761. https://doi.org/10.1063/1.1743626.

Evans, K.A., 2012. The redox budget of subduction zones. Earth-Science Reviews 113(1), 11-32. https://doi.org/10.1016/j.earscirev.2012.03.003.

Farsang, S., Zajacz, Z., 2025. Sulfur species and gold transport in arc magmatic fluids. Nature Geoscience. https://doi.org/10.1038/s41561-024-01601-3.

Ford, C.E., Russell, D.G., Craven, J.A., Fisk, M.R., 1983. Olivine-Liquid Equilibria: Temperature, Pressure and Composition Dependence of the Crystal/Liquid Cation Partition Coefficients for Mg, Fe2+, Ca and Mn. Journal of Petrology 24(3), 256-266. https://doi.org/10.1093/petrology/24.3.256.

Frost, B.R., 1991. Chapter 1. Introduction to oxygen fugacity and its petrologic importance, in: Lindsley, D.H. (Ed.) Oxide Minerals: Petrologic and Magnetic Significance. De Gruyter, Berlin, Boston, pp. 1-10. https://doi.org/10.1515/9781501508684-004.

Gaetani, G.A., Grove, T.L., 1997. Partitioning of moderately siderophile elements among olivine, silicate melt, and sulfide melt: Constraints on core formation in the Earth and Mars. Geochimica et Cosmochimica Acta 61(9), 1829-1846. https://doi.org/10.1016/S0016-7037(97)00033-1.

Gavrilenko, M., Batanova, V.G., Llovet, X., Krasheninnikov, S., Koshlyakova, A.N., Sobolev, A.V., 2023. Secondary fluorescence effect quantification of EPMA analyses of olivine grains embedded in basaltic glass. Chemical Geology 621, 121328-121328. https://doi.org/10.1016/j.chemgeo.2023.121328.

Gorman, J.K., Nardella, W.R., 1962. Hydrogen permeation through metals. Vacuum 12(1), 19-24. https://doi.org/10.1016/0042-207X(62)90821-7.

Guillong, M., Meier, D.L., Allan, M.M., Heinrich, C.A., Yardley, B.W.D., 2008. Appendix A6: SILLS: A MATLAB-based program for the reduction of laser ablation ICP-MS data of homogeneous materials and inclusions. Mineralogical Association of Canada Short Course 40, 328-333. https://doi.org/10.3749/9780921294801.app06.

Gunter, W.D., Myers, J., Wood, J.R., 1979. The Shaw bomb, an ideal hydrogen sensor. Contributions to Mineralogy and Petrology 70(1), 23-27. https://doi.org/10.1007/BF00371868.

Heinrich, C.A., 2024. The Chain of Processes Forming Porphyry Copper Deposits—An Invited Paper*. Economic Geology 119(4), 741-769. https://doi.org/10.5382/econgeo.5069.

Hewitt, D.A., 1977. Hydrogen fugacities in Shaw bomb experiments. Contributions to Mineralogy and Petrology 65(2), 165-169. https://doi.org/10.1007/BF00371056.

Jayasuriya, K.D., O'Neill, H.S.C., Berry, A.J., Campbell, S.J., 2004. A Mössbauer study of the oxidation state of Fe in silicate melts. American Mineralogist 89(11-12), 1597-1609. https://doi.org/10.2138/am-2004-11-1203.

Jenner, F.E., O'Neill, H.S.C., 2012. Major and trace analysis of basaltic glasses by laser-ablation ICP-MS. Geochemistry, Geophysics, Geosystems 13(3), n/a-n/a. https://doi.org/10.1029/2011GC003890.

Kelley, K.A., Cottrell, E., 2012. The influence of magmatic differentiation on the oxidation state of Fe in a basaltic arc magma. Earth and Planetary Science Letters 329-330, 109-121. https://doi.org/10.1016/j.epsl.2012.02.010.

Kress, V.C., Carmichael, I.S.E., 1991. The compressibility of silicate liquids containing Fe2O3 and the effect of composition, temperature, oxygen fugacity and pressure on their redox states. Contributions to Mineralogy and Petrology 108(1), 82-92. https://doi.org/10.1007/BF00307328.

Lanari, P., Vho, A., Bovay, T., Airaghi, L., Centrella, S., 2019. Quantitative compositional mapping of mineral phases by electron probe micro-analyser. Geological Society, London, Special Publications 478(1), 39-63. https://doi.org/10.1144/SP478.4.

Lanari, P., Vidal, O., De Andrade, V., Dubacq, B., Lewin, E., Grosch, E.G., Schwartz, S., 2014. XMapTools: A MATLAB©-based program for electron microprobe X-ray image processing and geothermobarometry. Computers & Geosciences 62, 227-240. https://doi.org/10.1016/j.cageo.2013.08.010.

Laubier, M., Grove, T.L., Langmuir, C.H., 2014. Trace element mineral/melt partitioning for basaltic and basaltic andesitic melts: An experimental and laser ICP-MS study with application to the oxidation state of mantle source regions. Earth and Planetary Science Letters 392, 265-278. https://doi.org/10.1016/j.epsl.2014.01.053.

Lawrence, I.K.L., 1989. A Concordance Correlation Coefficient to Evaluate Reproducibility. Biometrics 45(1), 255-268. https://doi.org/10.2307/2532051.

Lee, C.-T.A., Luffi, P., Chin, E.J., Bouchet, R., Dasgupta, R., Morton, D.M., Le Roux, V., Yin, Q.-z., Jin, D., 2012. Copper Systematics in Arc Magmas and Implications for Crust-Mantle Differentiation. Science 336(6077), 64 LP-68. https://doi.org/10.1126/science.1217313.

Lee, C.-T.A., Luffi, P., Le Roux, V., Dasgupta, R., Albaréde, F., Leeman, W.P., 2010. The redox state of arc mantle using Zn/Fe systematics. Nature 468(7324), 681-685. https://doi.org/10.1038/nature09617.

Lesne, P., Scaillet, B., Pichavant, M., Iacono-Marziano, G., Beny, J.-M., 2011. The H2O solubility of alkali basaltic melts: an experimental study. Contributions to Mineralogy and Petrology 162(1), 133-151. https://doi.org/10.1007/s00410-010-0588-x.

Leuthold, J., Blundy, J., Ulmer, P., 2023. Trace element partitioning in basaltic systems as a function of oxygen fugacity. Contributions to Mineralogy and Petrology 178(12), 95-95. https://doi.org/10.1007/s00410-023-02069-x.

Longerich, H.P., Jackson, S.E., Günther, D., 1996. Inter-laboratory note. Laser ablation inductively coupled plasma mass spectrometric transient signal data acquisition and analyte concentration calculation. Journal of Analytical Atomic Spectrometry 11(9), 899-904. https://doi.org/10.1039/JA9961100899.

Mallmann, G., Burnham, A.D., Fonseca, R.O.C., 2022. Mineral-Melt Partitioning of Redox-Sensitive Elements, Magma Redox Geochemistry. pp. 345-367. https://doi.org/10.1002/9781119473206.ch17.

Mallmann, G., O'Neill, H.S.C., 2009. The Crystal/Melt Partitioning of V during Mantle Melting as a Function of Oxygen Fugacity Compared with some other Elements (Al, P, Ca, Sc, Ti, Cr, Fe, Ga, Y, Zr and Nb). Journal of Petrology 50(9), 1765-1794. https://doi.org/10.1093/petrology/egp053.

Mallmann, G., O'Neill, H.S.C., 2013. Calibration of an Empirical Thermometer and Oxybarometer based on the Partitioning of Sc, Y and V between Olivine and Silicate Melt. Journal of Petrology 54(5), 933-949. https://doi.org/10.1093/petrology/egt001.

Marquardt, D.W., 1963. An Algorithm for Least-Squares Estimation of Nonlinear Parameters. Journal of the Society for Industrial and Applied Mathematics 11(2), 431-441. https://doi.org/10.1137/0111030.

Marxer, F., Ulmer, P., Müntener, O., 2021. Polybaric fractional crystallisation of arc magmas: an experimental study simulating trans-crustal magmatic systems. Contributions to Mineralogy and Petrology 177(1), 3-3. https://doi.org/10.1007/s00410-021-01856-8.

Matzen, A.K., Baker, M.B., Beckett, J.R., Stolper, E.M., 2011. Fe−Mg Partitioning between Olivine and High-magnesian Melts and the Nature of Hawaiian Parental Liquids. Journal of Petrology 52(7-8), 1243-1263. https://doi.org/10.1093/petrology/egq089.

Matzen, A.K., Woodland, A., Beckett, J.R., Wood, B.J., 2022. Oxidation state of iron and Fe-Mg partitioning between olivine and basaltic martian melts. 107(7), 1442-1452. https://doi.org/doi:10.2138/am-2021-7682.

Métrich, N., 2022. Redox State of Volatiles and Their Relationships with Iron in Silicate Melts, Magma Redox Geochemistry. pp. 215-232. https://doi.org/10.1002/9781119473206.ch11.

Moré, J.J., 1978. The Levenberg-Marquardt algorithm: Implementation and theory, in: Watson, G.A. (Ed.) Numerical Analysis. Springer Berlin Heidelberg, Berlin, Heidelberg, pp. 105-116. https://doi.org/10.1007/BFb0067700.

Moretti, R., Neuville, D.R., 2022. Redox Equilibria, Magma Redox Geochemistry. pp. 1-17. https://doi.org/10.1002/9781119473206.ch1.

Moretti, R., Ottonello, G., 2022. Silicate Melt Thermochemistry and the Redox State of Magmas. Reviews in Mineralogy and Geochemistry 87(1), 339-403. https://doi.org/10.2138/rmg.2022.87.08.

Motulsky, H., Christopoulos, A., 2004. Fitting Models to Biological Data Using Linear and Nonlinear Regression: A practical guide to curve fitting. Oxford University Press. https://doi.org/10.1093/oso/9780195171792.001.0001.

Muan, A., Osborn, E.F., 1956. Phase Equilibria at Liquidus Temperatures in the System MgO-FeO-Fe2O3-SiO2. Journal of the American Ceramic Society 39(4), 121-140. https://doi.org/10.1111/j.1151-2916.1956.tb14178.x.

Mysen, B.O., 2006. Redox equilibria of iron and silicate melt structure: Implications for olivine/melt element partitioning. Geochimica et Cosmochimica Acta 70(12), 3121-3138. https://doi.org/10.1016/j.gca.2006.03.014.

Mysen, B.O., Richet, P., 2005. Silicate Glasses and Melts: Properties and Structure. Elsevier, Amsterdam, Boston, London, New York, Oxford, Paris, San Diego, San Francisco, Singapore, Sydney, Tokyo. https://doi.org/10.1016/S0921-3198(05)X8001-2.

Mysen, B.O., Virgo, D., Seifert, F.A., 1982. The structure of silicate melts: Implications for chemical and physical properties of natural magma. Reviews of Geophysics 20(3), 353-383. https://doi.org/10.1029/RG020i003p00353.

Nandedkar, R.H., 2014. Thesis: Evolution of hydrous mantle-derived calc-alkaline liquids by fractional crystallization at 0.7 and 0.4 GPa: An experimental study. ETH Zurich.

1231   Nandedkar, R.H., Ulmer, P., Müntener, O., 2014. Fractional crystallization of primitive,
1232 hydrous arc magmas: an experimental study at 0.7 GPa. Contributions to Mineralogy and Petrology
1233 167(6), 1015-1015. https://doi.org/10.1007/s00410-014-1015-5.

1234   Ni, H., Hui, H., Steinle-Neumann, G., 2015. Transport properties of silicate melts. Reviews
1235 of Geophysics 53(3), 715-744. https://doi.org/10.1002/2015RG000485.

1236   OriginLab, 2024. OriginPro (Version 2024 Academic) OriginLab Corporation.

1237   Osborn, E.F., 1959. Role of oxygen pressure in the crystallization and differentiation of
1238 basaltic magma. American Journal of Science 257(9), 609 LP-647.
1239 https://doi.org/10.2475/ajs.257.9.609.

1240   Papike, J.J., Burger, P.V., Bell, A.S., Le, L., Shearer, C.K., Sutton, S.R., Jones, J., Newville,
1241 M., 2013. Developing vanadium valence state oxybarometers (spinel-melt, olivine-melt, spinel-
1242 olivine) and V/(Cr+Al) partitioning (spinel-melt) for martian olivine-phyric basalts. American
1243 Mineralogist 98(11-12), 2193-2196. https://doi.org/10.2138/am.2013.4622.

1244   Park, J.-W., Campbell, I.H., Chiaradia, M., Hao, H., Lee, C.-T., 2021. Crustal magmatic
1245 controls on the formation of porphyry copper deposits. Nature Reviews Earth & Environment 2(8),
1246 542-557. https://doi.org/10.1038/s43017-021-00182-8.

1247   Paton, C., Hellstrom, J., Paul, B., Woodhead, J., Hergt, J., 2011. Iolite: Freeware for the
1248 visualisation and processing of mass spectrometric data. Journal of Analytical Atomic Spectrometry
1249 26(12), 2508-2518. https://doi.org/10.1039/C1JA10172B.

1250   Pirrie, D., Butcher, A.R., Power, M.R., Gottlieb, P., Miller, G.L., 2004. Rapid quantitative
1251 mineral and phase analysis using automated scanning electron microscopy (QemSCAN); potential
1252 applications in forensic geoscience, in: Pye, K., Croft, D.J. (Eds.), Forensic Geoscience: Principles,
1253 Techniques and Applications. Geological Society of London, p. 0.
1254 https://doi.org/10.1144/gsl.Sp.2004.232.01.12.

1255   Putirka, K., 2016. Rates and styles of planetary cooling on Earth, Moon, Mars, and Vesta,
1256 using new models for oxygen fugacity, ferric-ferrous ratios, olivine-liquid Fe-Mg exchange, and
1257 mantle potential temperature. American Mineralogist 101(4), 819-840. https://doi.org/10.2138/am-
1258 2016-5402.

1259   Rauchenstein-Martinek, K., Wagner, T., Wälle, M., Heinrich, C.A., 2014. Gold concentrations
1260 in metamorphic fluids: A LA-ICPMS study of fluid inclusions from the Alpine orogenic belt. Chemical
1261 Geology 385, 70-83. https://doi.org/10.1016/j.chemgeo.2014.07.018.

1262   Richards, J.P., 2015. The oxidation state, and sulfur and Cu contents of arc magmas:
1263 implications for metallogeny. Lithos 233, 27-45. https://doi.org/10.1016/j.lithos.2014.12.011.

1264   Roeder, P.L., Emslie, R.F., 1970. Olivine-Liquid Equilibrium. Contributions to Mineralogy and
1265 Petrology, 29 (4): 275-289.

1266   Saper, L.M., Baker, M.B., Stolper, E.M., 2022. Fe2+−Mg partitioning between olivine and
1267 liquid at low oxygen fugacity: an experimental and thermodynamic framework. Contributions to
1268 Mineralogy and Petrology 177(10), 94-94. https://doi.org/10.1007/s00410-022-01955-0.

1269   Sato, M., 1978. Oxygen fugacity of basaltic magmas and the role of gas-forming elements.
1270 Geophysical Research Letters 5(6), 447-449. https://doi.org/10.1029/GL005i006p00447.

1271   Scaillet, B., Pichavant, M., Roux, J., Humbert, G., Lefevre, A., 1992. Improvements of the
1272 Shaw membrane technique for measurement and control of fH2 at high temperatures and pressures.
1273 American Mineralogist 77(5-6), 647-655.

1274   Schindelin, J., Arganda-Carreras, I., Frise, E., Kaynig, V., Longair, M., Pietzsch, T.,
1275 Preibisch, S., Rueden, C., Saalfeld, S., Schmid, B., Tinevez, J.-Y., White, D.J., Hartenstein, V.,
1276 Eliceiri, K., Tomancak, P., Cardona, A., 2012. Fiji: an open-source platform for biological-image
1277 analysis. Nature Methods 9(7), 676-682. https://doi.org/10.1038/nmeth.2019.

Shaw, H.R., 1963. Hydrogen-Water Vapor Mixtures: Control of Hydrothermal Atmospheres by Hydrogen Osmosis. Science 139(3560), 1220 LP-1222. https://doi.org/10.1126/science.139.3560.1220.

Shea, T., Ruth, D., Jollands, M., Ohtaki, K., Ishii, H., Bradley, J., 2023. The presence of silicate melt may enhance rates of cation diffusion in olivine. Earth and Planetary Science Letters 621, 118370. https://doi.org/10.1016/j.epsl.2023.118370.

Shearer, C.K., McKay, G., Papike, J.J., Karner, J.M., 2006. Valence state partitioning of vanadium between olivine-liquid: Estimates of the oxygen fugacity of Y980459 and application to other olivine-phyric martian basalts. American Mineralogist 91(10), 1657-1663. https://doi.org/10.2138/am.2006.2155.

Shishkina, T.A., Portnyagin, M.V., Botcharnikov, R.E., Almeev, R.R., Simonyan, A.V., Garbe-Schönberg, D., Schuth, S., Oeser, M., Holtz, F., 2018. Experimental calibration and implications of olivine-melt vanadium oxybarometry for hydrous basaltic arc magmas. American Mineralogist 103(3), 369-383. https://doi.org/10.2138/am-2018-6210.

Sillitoe, R.H., 2010. Porphyry copper systems. Economic Geology 105(1), 3-41. https://doi.org/10.2113/gsecongeo.105.1.3.

Stanley, C.R., Lawie, D., 2007. Average Relative Error in Geochemical Determinations: Clarification, Calculation, and a Plea for Consistency. Exploration and Mining Geology 16(3-4), 267-275. https://doi.org/10.2113/gsemg.16.3-4.267.

Tang, M., Erdman, M., Eldridge, G., Lee, C.-T.A., 2018. The redox "filter" beneath magmatic orogens and the formation of continental crust. Science Advances 4(5). https://doi.org/10.1126/sciadv.aar4444.

Tassara, S., Reich, M., Cannatelli, C., Konecke, B.A., Kausel, D., Morata, D., Barra, F., Simon, A.C., Fiege, A., Morgado, E., Leisen, M., 2020. Post-melting oxidation of highly primitive basalts from the southern Andes. Geochimica et Cosmochimica Acta 273, 291-312. https://doi.org/10.1016/j.gca.2020.01.042.

Toplis, M.J., 2005. The thermodynamics of iron and magnesium partitioning between olivine and liquid: criteria for assessing and predicting equilibrium in natural and experimental systems. Contributions to Mineralogy and Petrology 149(1), 22-39. https://doi.org/10.1007/s00410-004-0629-4.

Tuff, J., O'Neill, H.S.C., 2010. The effect of sulfur on the partitioning of Ni and other first-row transition elements between olivine and silicate melt. Geochimica et Cosmochimica Acta 74(21), 6180-6205. https://doi.org/10.1016/j.gca.2010.08.014.

Ulmer, P., 1989. The dependence of the Fe^{2+}-Mg cation-partitioning between olivine and basaltic liquid on pressure, temperature and composition. Contributions to Mineralogy and Petrology 101(3), 261-273. https://doi.org/10.1007/BF00375311.

van Gerve, T.D., Namur, O., 2023. SilicH2O: a graphical user interface for processing silicate glass Raman spectra and quantifying H2O. Volcanica 6(2), 405–413. https://doi.org/10.30909/vol.06.02.405413.

Wang, J., Xiong, X., Takahashi, E., Zhang, L., Li, L., Liu, X., 2019. Oxidation State of Arc Mantle Revealed by Partitioning of V, Sc, and Ti Between Mantle Minerals and Basaltic Melts. Journal of Geophysical Research: Solid Earth 124(5), 4617-4638. https://doi.org/10.1029/2018JB016731.

Wilkinson, J.J., 2013. Triggers for the formation of porphyry ore deposits in magmatic arcs. Nature Geoscience 6(11), 917-925. https://doi.org/10.1038/ngeo1940.

Zajacz, Z., Candela, P.A., Piccoli, P.M., Sanchez-Valle, C., 2012. The partitioning of sulfur and chlorine between andesite melts and magmatic volatiles and the exchange coefficients of major cations. Geochimica et Cosmochimica Acta 89, 81-101. https://doi.org/10.1016/j.gca.2012.04.039.

1326 Zajacz, Z., Halter, W., Malfait, W.J., Bachmann, O., Bodnar, R.J., Hirschmann, M.M.,
1327 Mandeville, C.W., Morizet, Y., Müntener, O., Ulmer, P., Webster, J.D., 2005. A composition-
1328 independent quantitative determination of the water content in silicate glasses and silicate melt
1329 inclusions by confocal Raman spectroscopy. Contributions to Mineralogy and Petrology 150(6), 631-
1330 642. https://doi.org/10.1007/s00410-005-0040-9.

1331 Zajacz, Z., Seo, J.H., Candela, P.A., Piccoli, P.M., Tossell, J.A., 2011. The solubility of
1332 copper in high-temperature magmatic vapors: A quest for the significance of various chloride and
1333 sulfide complexes. Geochimica et Cosmochimica Acta 75(10), 2811-2827.
1334 https://doi.org/10.1016/j.gca.2011.02.029.

1335 Zajacz, Z., Tsay, A., 2019. An accurate model to predict sulfur concentration at anhydrite
1336 saturation in silicate melts. Geochimica et Cosmochimica Acta 261, 288-304.
1337 https://doi.org/10.1016/j.gca.2019.07.007.

1338 Zanetti, A., Tiepolo, M., Oberti, R., Vannucci, R., 2004. Trace-element partitioning in olivine:
1339 modelling of a complete data set from a synthetic hydrous basanite melt. Lithos 75(1), 39-54.
1340 https://doi.org/10.1016/j.lithos.2003.12.022.

1341 Zhao, S.-Y., Yang, A.Y., Langmuir, C.H., Zhao, T.-P., 2022. Oxidized primary arc magmas:
1342 Constraints from Cu/Zr systematics in global arc volcanics. Science Advances 8(12), eabk0718-
1343 eabk0718. https://doi.org/10.1126/sciadv.abk0718.

1344

Figure captions

1346 **Fig. 1.** An example of LA-ICP-MS analysis of olivines. a) Typical ablation scenarios:
1347 1) pure olivine ablation until glass matrix is reached underneath; 2) contamination of the
1348 ablation by a spinel inclusion; and 3) irregularities of olivine's geometry in depth lead to
1349 early contamination of the signal by the silicate glass matrix. b) Typical LA-ICP-MS signal
1350 of olivine showing scenario 2 with spinel inclusion and the onset of glass ablation. c)
1351 Backscattered electron (BSE) image of the laser pit in olivine.

1352

1353 **Fig. 2.** Time series experiments reflecting Ol-melt equilibrium via a) $\log(K_{D[Fe_T/Mg]}^{[Ol/melt]})$ and
1354 b) $\log(K_{D[V/Sc]}^{[Ol/melt]})$. The time series was carried out at fO_2 ~FMQ +2.5, T = 960 °C.

1355

1356 **Fig. 3.** Iron intensity distribution maps (WDX-EPMA) in olivines for representative
1357 samples (a) E1.1_IV_A (fO_2 = FMQ +3.56, T = 990 °C) and (b) E7.0_II_SB_A (fO_2 = FMQ -
1358 0.87, T = 1019 °C). From left to right BSE-image and Fe-map are displayed with relative
1359 intensities denoted by the accompanying color bar, demonstrating consistent chemical
1360 homogeneity. The bright rim visible between the glass matrix and the olivine is due to the
1361 topographic contrast effects. Mineral abbreviations: olivine (Ol), plagioclase (Pl) and spinel
1362 (Spl).

1363

1364   **Fig. 4.** Experimental run products of the MKCA series of the E7.X_SB-fO$_2$-LLD
1365 (~FMQ -1) shown in BSE-images. Olivine is present in addition to a variety of other mineral
1366 phases. Mineral abbreviations as in Fig. 3. Additional abbreviations: amphibole, (Amp),
1367 apatite (Ap), clinopyroxene (Cpx), glass (Gl), ilmenite (Ilm), and orthopyroxene (Opx).

1368

1369   **Fig. 5.** Summary of the behavior of V and Sc as a function of logfO_2 in olivine and
1370 silicate melt. a) to d): $\log(D_{[V]}^{[Ol/melt]})$, $\log(K_{D[V/Sc]}^{[Ol/melt]})$, $\log(D_{[Sc]}^{[Ol/melt]})$ and V-content as a function of
1371 logfO_2 (ΔFMQ), respectively. For all fits: p < 0.0001. In a) and b) linear fitting was applied.
1372 Experiment E7.3_SB_A is considered as an outlier with respect to the $\log(D_{[V]}^{[Ol/melt]})$ and
1373 therefore excluded from the linear regression in panel (a). The quality of the fit is expressed
1374 by high coefficient of determination (R^2) and very low root mean squared error (RMSE)
1375 values. b) to d): Symbol rims are color coded depending on the degree of polymerization
1376 expressed via the ratio of nonbridging oxygen per tetrahedrally coordinated cations (NBO/T).
1377 Liner fit (purple line) in panel (a) with fixed intercept derived from exploratory fitting on
1378 $D_{[V]}^{[Ol/melt]}$ as a function of fO_2 revealed the best fitting equation (for further details see
1379 supplementary material S1).

1380

1381   **Fig. 6.** Summary of the behavior of Fe and Mg as a function of logfO_2 in olivine and
1382 silicate melt. a) and b): The $\log(K_{D[Fe_T/Mg]}^{[Ol/melt]})$ versus logfO_2(ΔFMQ) with sigmoidal fitting. For all
1383 fits: p < 0.0001. a): Comparison of multiple sigmoidal fitting for subset of data: 1) only MKCA
1384 2) only SHOSH 3) all combined 4) all combined except of significant outliers (*). b) Display
1385 of modeled Fe-Mg exchange coefficient between olivine and melt ($\log(K_{D[Fe_T/Mg]}^{[Ol/melt]})_{mod}$) based on
1386 NBO/T and molar fraction of fayalite in olivine (X_{Fay}). For further details, see the main text.
1387 d) and c): FeO and MgO (in olivine and glass) as a function of logfO_2(ΔFMQ), respectively.

1388

1389   **Fig. 7.** Corrected Fe-Mg exchange coefficient between olivine and melt (
1390 $\log(K_{D[Fe_T/Mg]}^{[Ol/melt]})cor$) as a function of log$fO_2$. The applied sigmoidal regression line (p < 0.0001)
1391 serves as a Fe-Mg-oxybarometer for olivine silicate melt pairs, as defined by Eq. (7).

1392

1393   **Fig. 8.** Comparison of $\log(D_{[V]}^{[Ol/melt]})$ from published and current study data (TS, this

1394   study) as a function of $\log fO_2$. For all fits: $p < 0.0001$. a) Sigmoidal fit to the pre-filtered data

1395   (see supplement Table S.17 for details on data filtering, Outliers* marked by elliptical

1396   circles). b) Relevant distribution of V partitioning for terrestrial redox system. A comparison

1397   between linear fitting (blue, n = 149) and sigmoidal fitting (red, n = 167) from panel (a) is

1398   presented. The pink dashed-dotted line derives from linear regression fit from Eq. (3).

1399   Source of previous experimental data: Canil, 1997, 1999; Gaetani and Grove, 1997; Canil

1400   and Fedortchouk, 2001; Zanetti et al., 2004; Mallmann and O'Neill, 2009, 2013; Tuff and

1401   O'Neill, 2010; Papike et al., 2013; Laubier et al., 2014; Shishkina et al., 2018; Wang et al.,

1402   2019; Dygert et al., 2020; Leuthold et al., 2023; Erdmann et al., 2024.

1403

1404   **Fig. 9.** Comparison of $\log(K_{D[V/Sc]}^{[Ol/melt]})$ and $\log(D_{[Sc]}^{[Ol/melt]})$ from published and current study

1405   data as a function of $\log fO_2$ and temperature, respectively. For all fits: $p < 0.0001$ a)

1406   Sigmoidal fit to the pre-filtered data (see supplement Table S.17 for details on data filtering,

1407   Outliers* marked by elliptical circles). Apparent is a parallel offset for experiments of this

1408   study at very low NBO/T values. b) Accounting for the effect of NBO/T on $\log(D_{[Sc]}^{[Ol/melt]})$ while

1409   capturing its temperature influence, the $\log(D_{[Sc]}^{[Ol/melt]})$ demonstrates moderate exponential

1410   increase with decreasing temperature and NBO/T. Note increased scattering for anhydrous

1411   experiments. For further details, see the main text. Source of previous (V-Sc) experimental

1412   data: Canil and Fedortchouk, 2001; Zanetti et al., 2004; Mallmann and O'Neill, 2009, 2013;

1413   Tuff and O'Neill, 2010; Laubier et al., 2014; Shishkina et al., 2018; Wang et al., 2019; Dygert

1414   et al., 2020; Leuthold et al., 2023; Erdmann et al., 2024. Sigmoidal fit through dataset from

1415   this study including fixed asymptote values based (horizontal dashed blue lines) on an

1416   apparent parallel shift compared to previous experiment at higher NBO/T values.

1417

1418   **Fig. 10.** Comparison of calculated Fe^{3+}/Fe_{tot} ratios in silicate melt derived from the

1419 $\log(K_{D[Fe/Mg]}^{[Ol/melt]})$ in this study with values predicted by different empirical models. The Fe^{3+}/Fe_{tot}

1420   ratios were calculated using the K_D-models of Toplis (2005) and Blundy et al. (2020).

1421   Uncertainties on these calculated Fe^{3+}/Fe_{tot} ratios are based on the 1σ calibration

1422   uncertainty in K_D (±0.03 for both models) combined with error propagation from calculated

1423   exchange coefficient and analytical uncertainties on Fe and Mg concentrations in both

1424   olivine and glass. The pink dashed line indicates a ratio value of zero. Predicted values are

1425   shown as lines derived from the empirical models (Kress and Carmichael, 1991; Jayasuriya

1426   et al., 2004; Putirka, 2016; Borisov et al., 2018). Literature (Lit.) values used as input for

1427 these prediction models correspond to the same experiments shown in Fig. 8, but with Fe-
1428 Mg-exchange data obtained from the original experimental studies.

1429

1430   **Fig. 11.** Accuracy and precision assessment of existing Ol-melt oxybarometers.
1431 Comparison between measured and calculated log$f$O$_2$ (both expressed as ΔFMQ). Vertical
1432 error bars represent 1σ propagated uncertainty based on analytical uncertainties (i.e., V-
1433 and Sc- concentrations) and errors of the fitting parameters except for studies where an
1434 equation was given to calculate the errors as 1σ (Shishkina et al. 2018; Erdmann et al.
1435 2024). 1) Dataset includes all experiments of this study with except for outlier E7.3_SB_A
1436 (n = 31). 2) Existing V-based oxybarometers were tested from previous studies (Canil and
1437 Fedortchouk, 2001; Mallmann and O'Neill, 2013; Shishkina et al., 2018; Wang et al., 2019;
1438 Erdmann et al., 2024). 3) The most promising oxybarometers were applied on an extended
1439 experimental dataset (FMQ -5 to +5, n = 345) to evaluate potential overfitting.

1440

1441   **Fig. 12.** Statistical comparison of different olivine-melt oxybarometers presented in
1442 Fig. 11. a) Quantitative assessment of each oxybarometer's precision and accuracy using
1443 the concordance correlation coefficient (CCC). For more details see the main text. b) RMSE
1444 values for each linear fit. c) Median uncertainty (2σ) when applying each oxybarometer to
1445 its respective dataset. Superscripts correspond to those in Fig. 11.

1446

1447 **Figures**
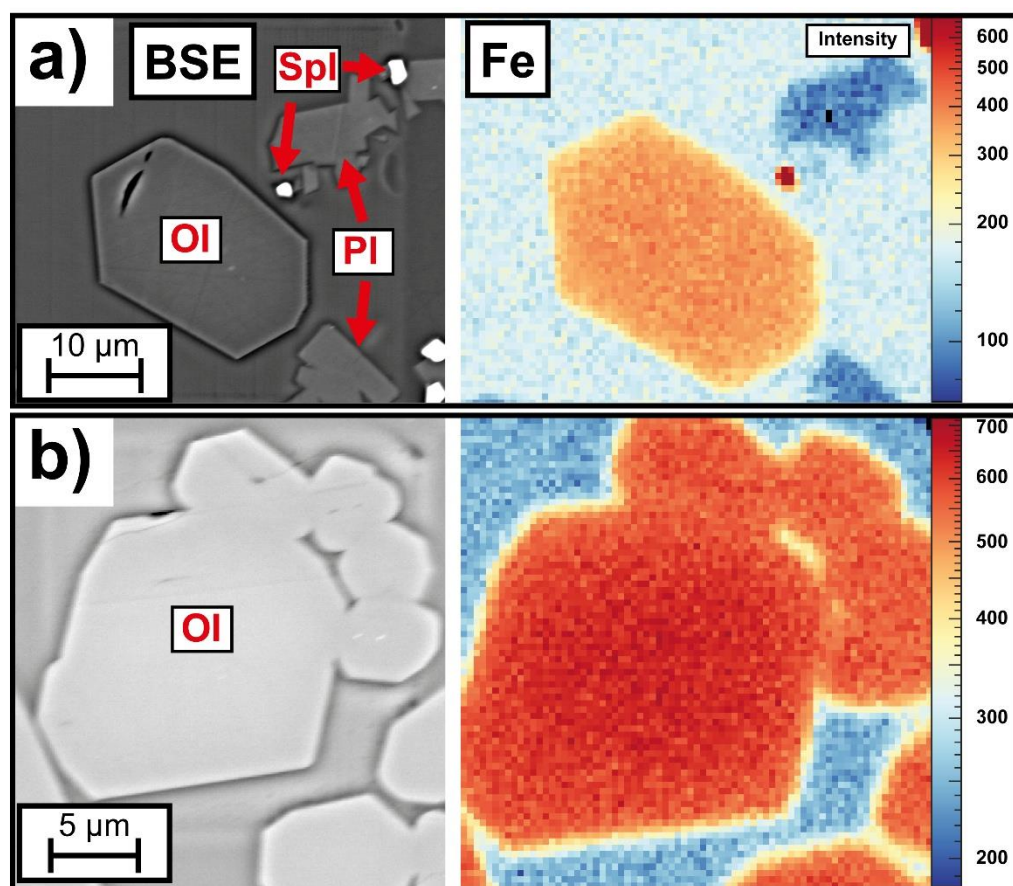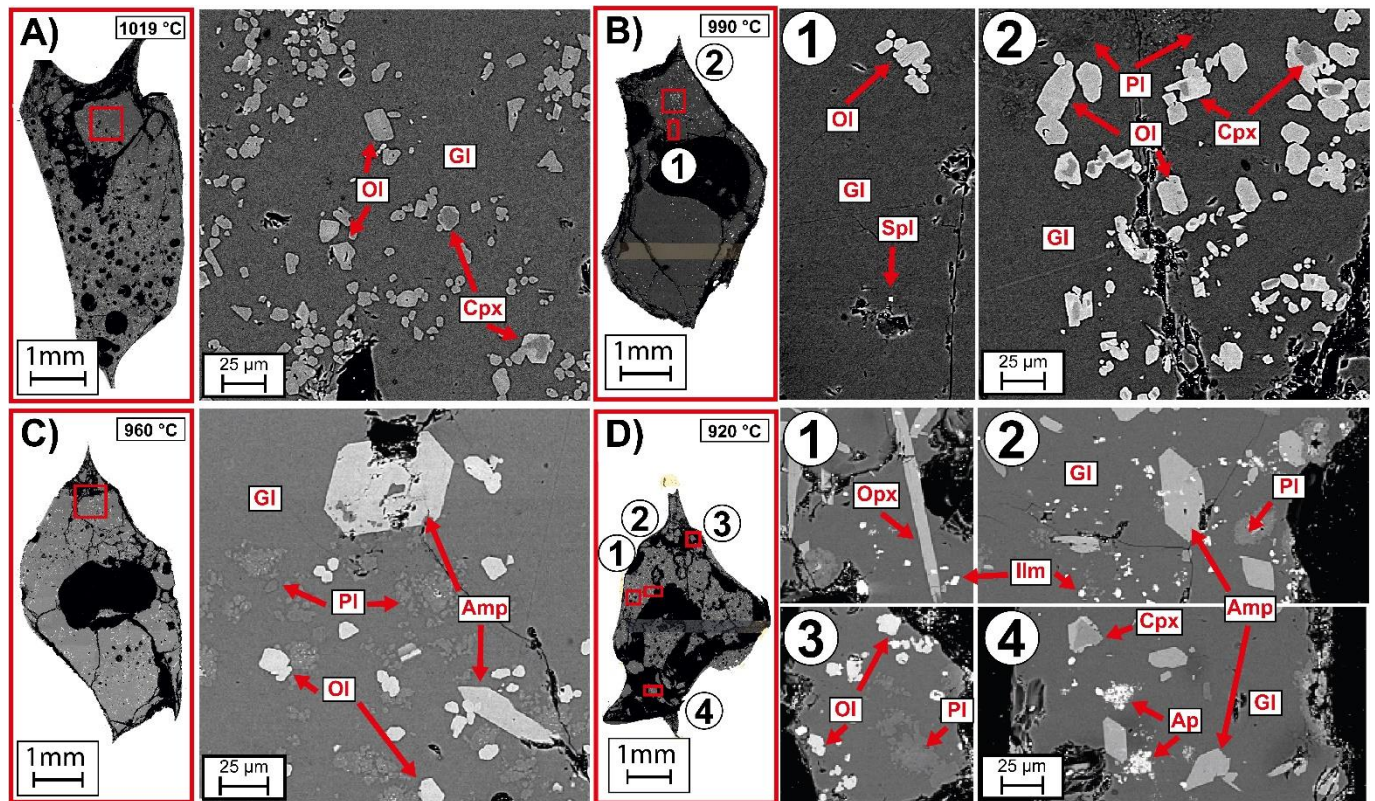
1448 Figure 1

1449

1450 Figure 2

1451
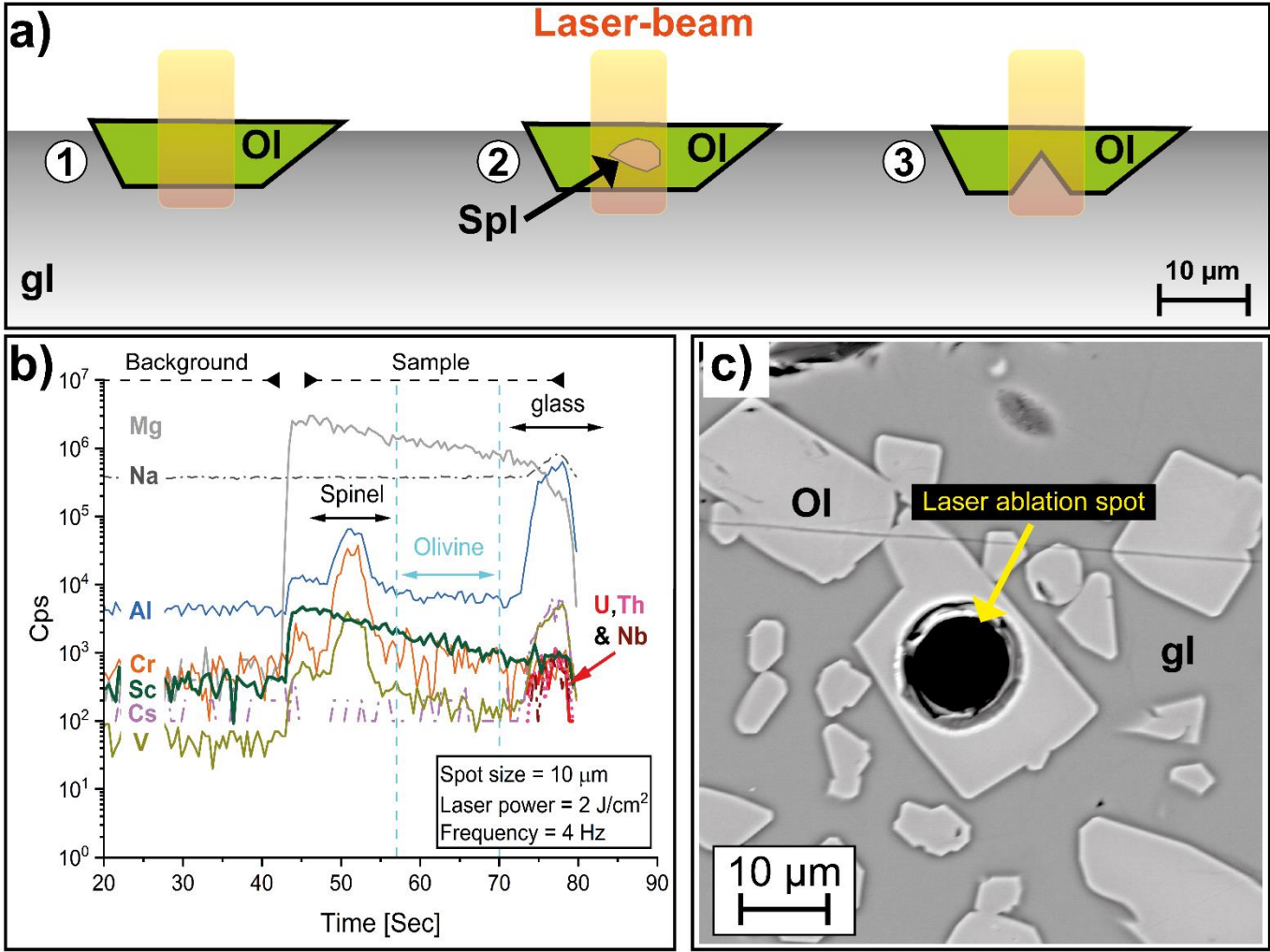
1452
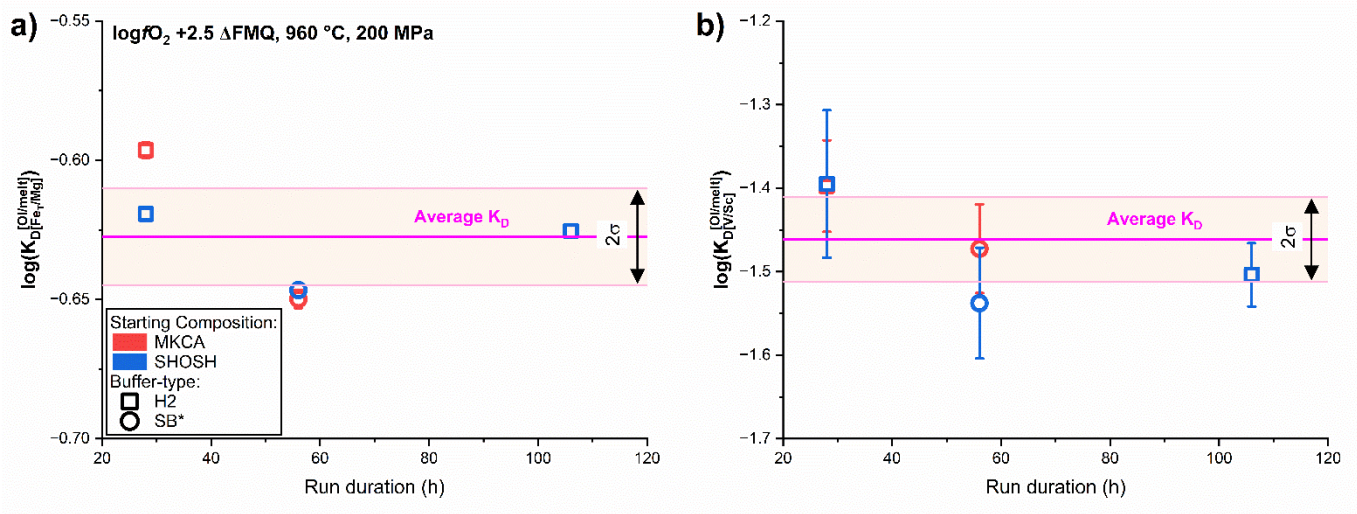
1453   Figure 3
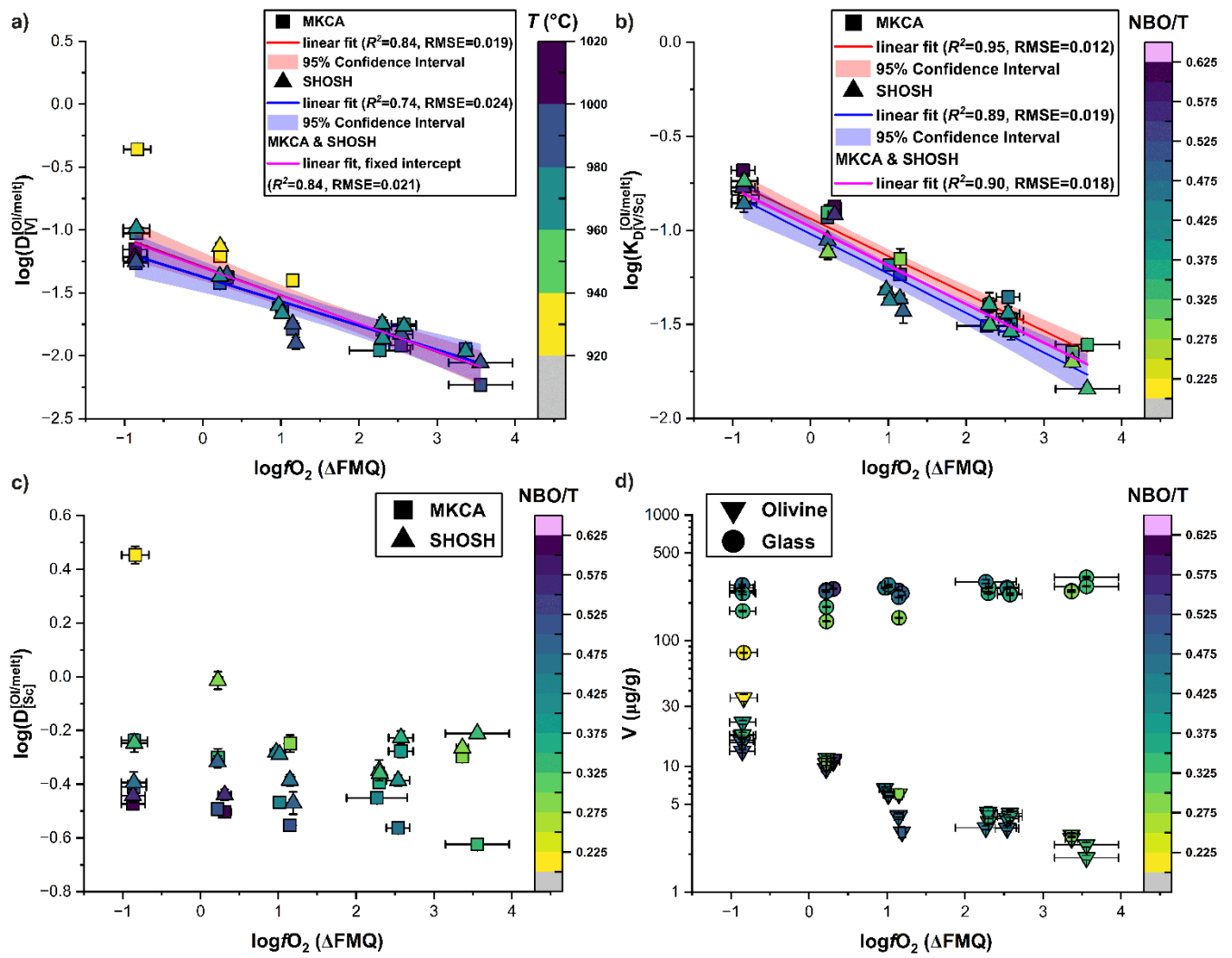

1454

1455

1456   Figure 4

1457

1458

1459   Figure 5

1460

1461

1462   Figure 6

1463

1464
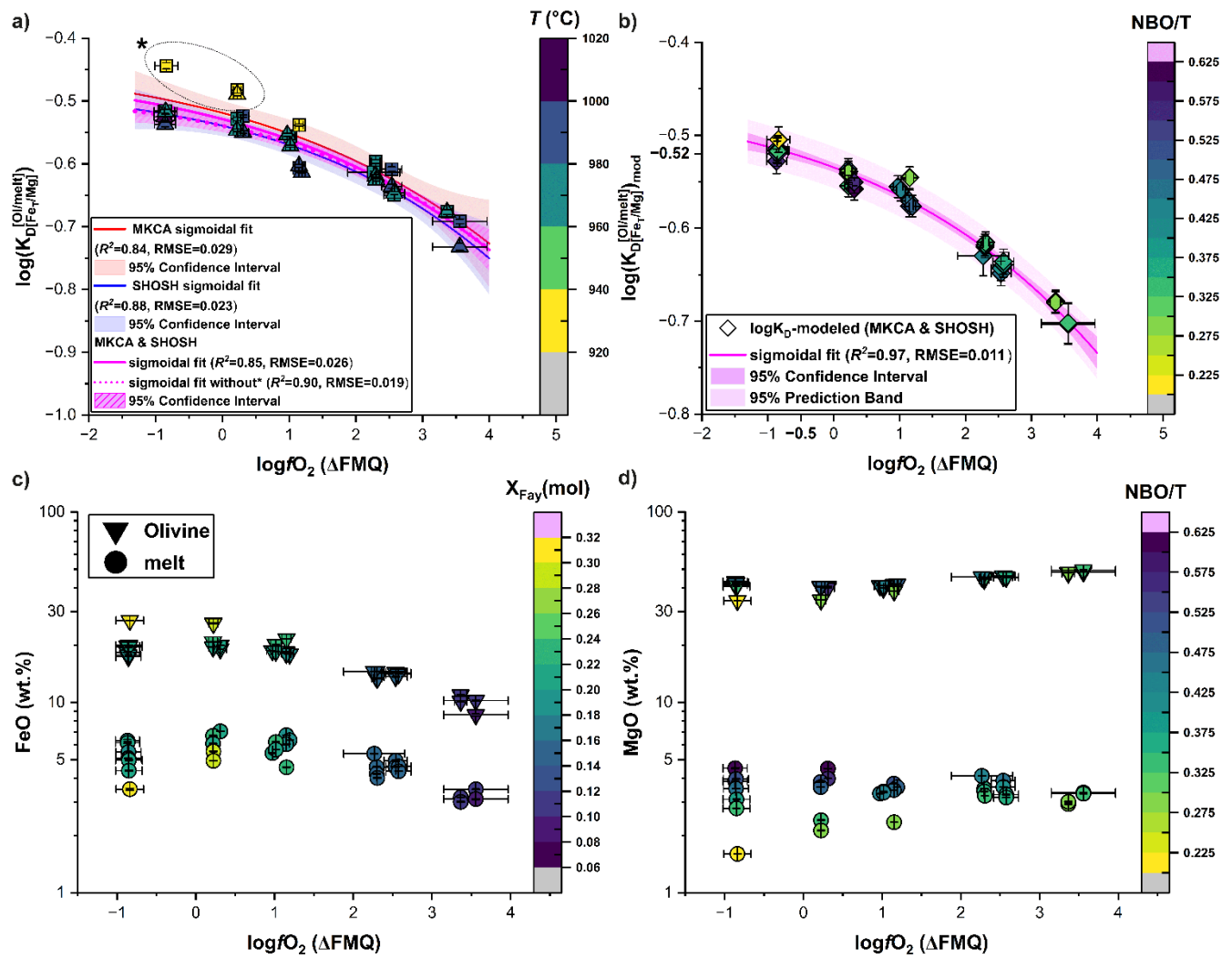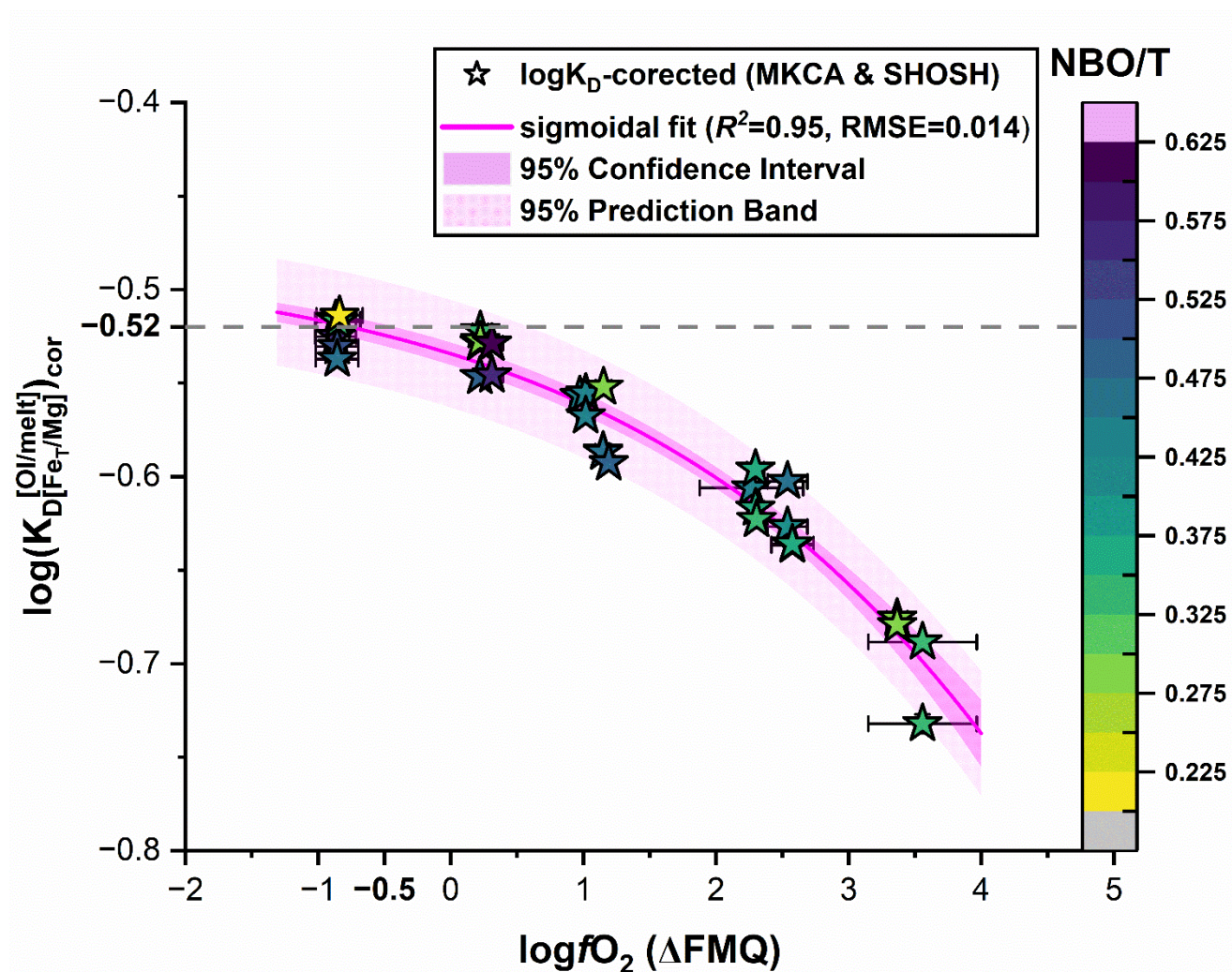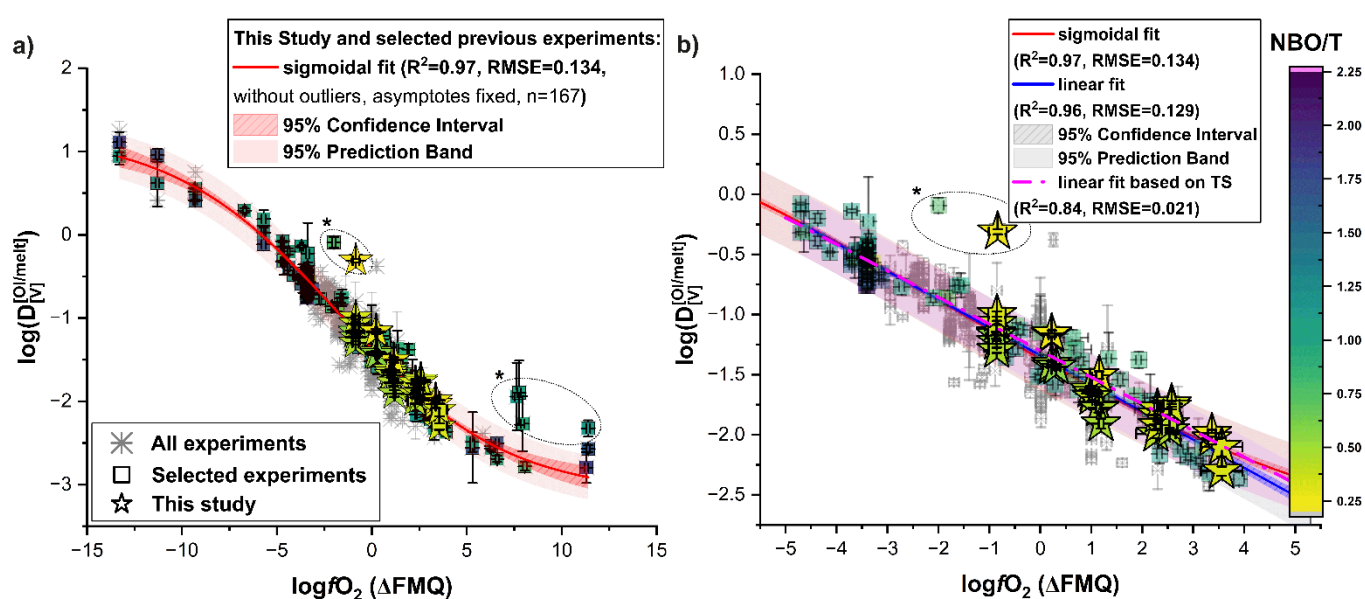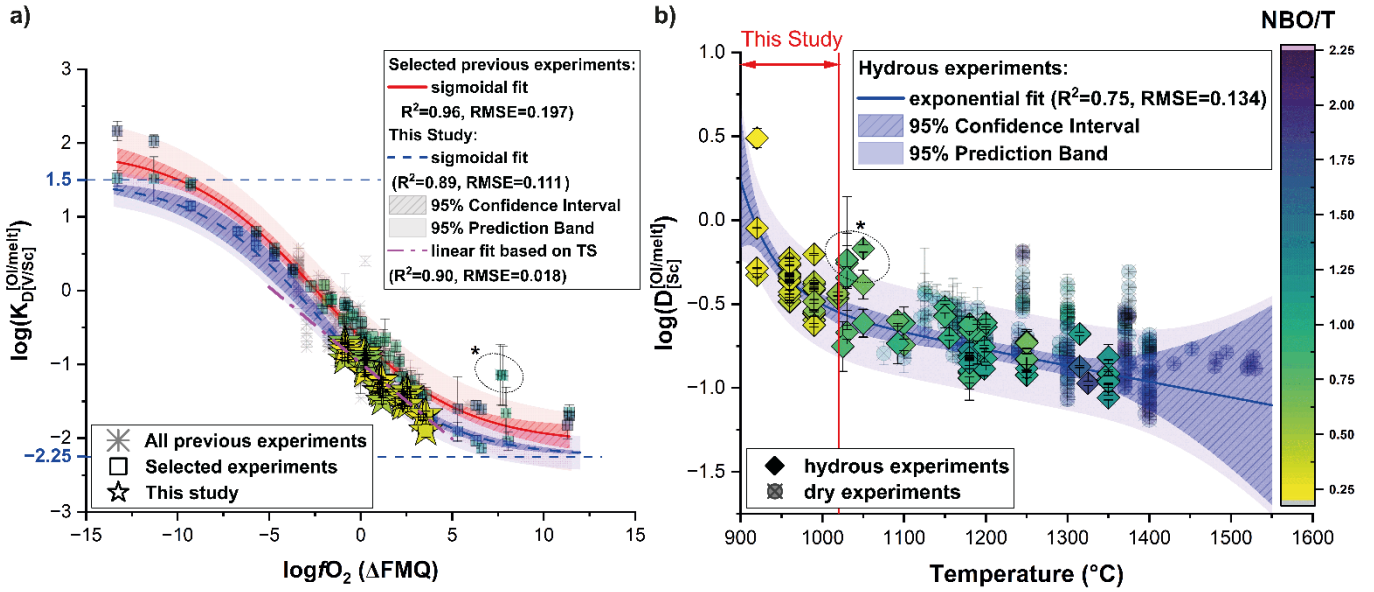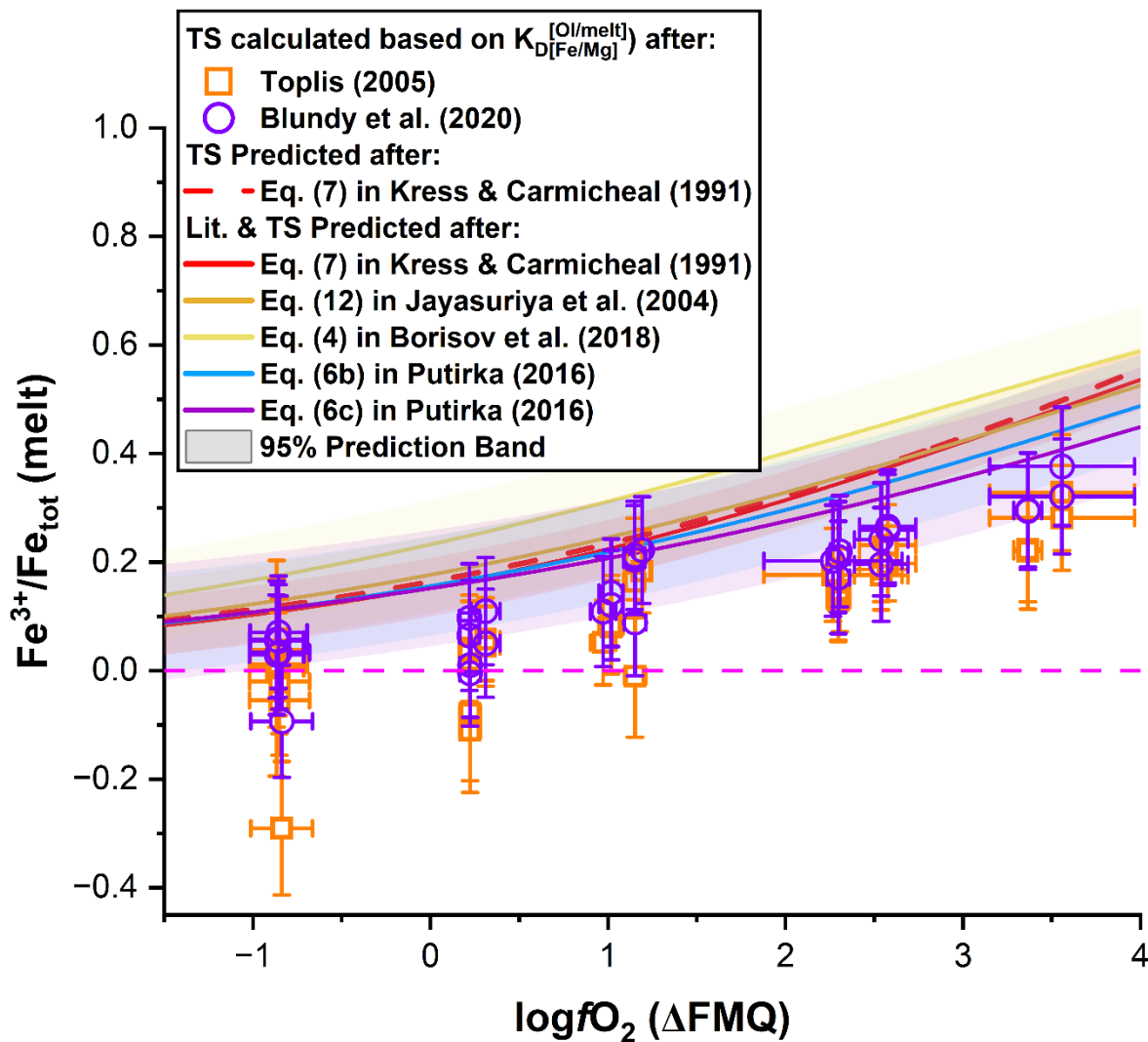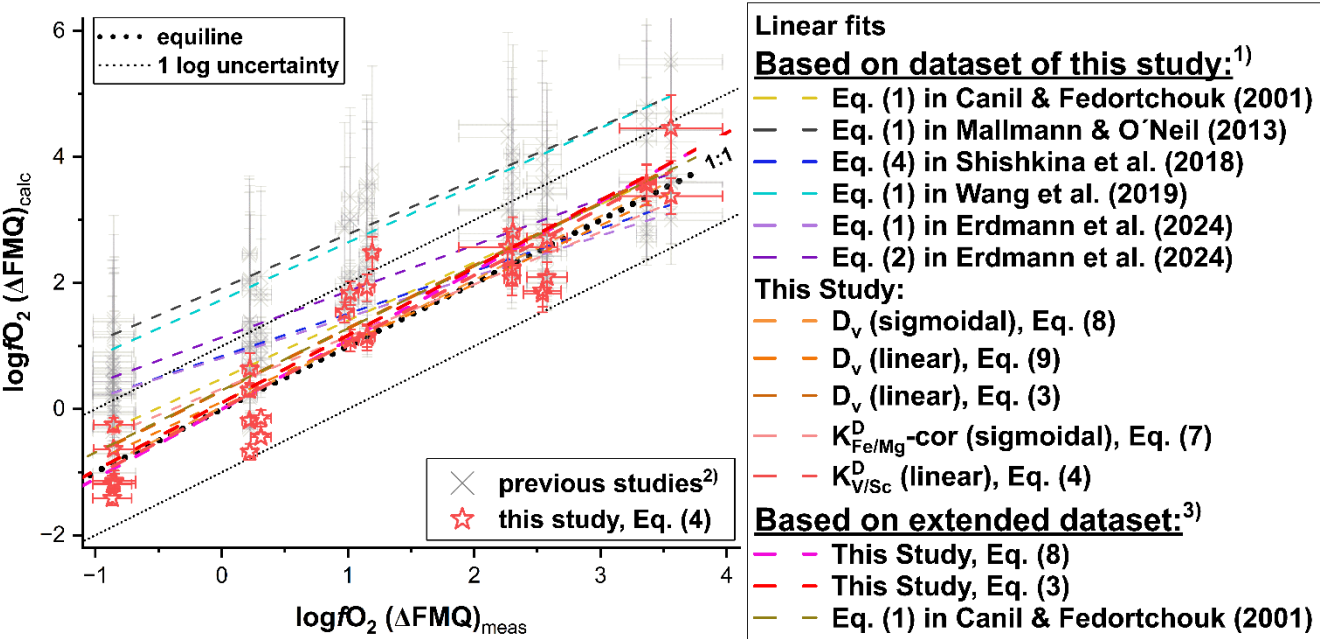
1465   Figure 7

1466

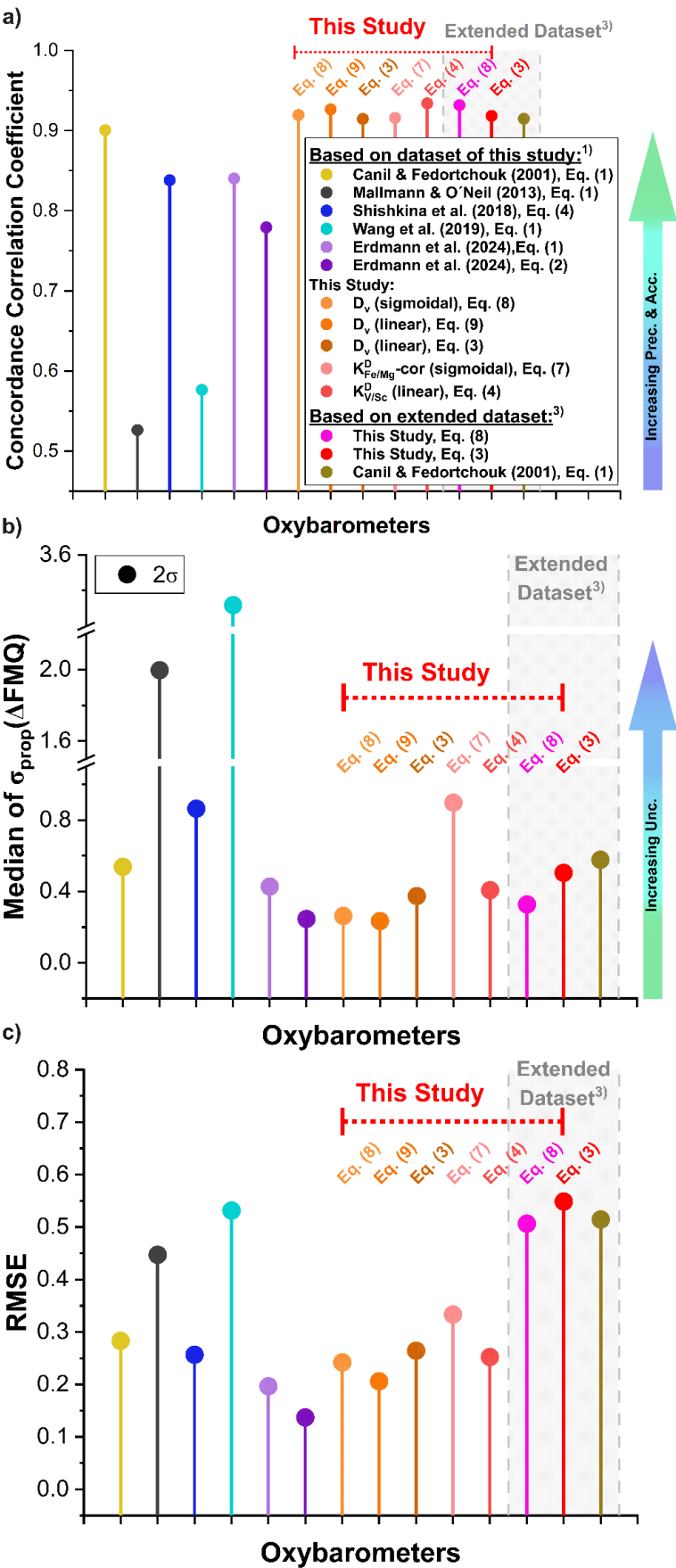1467   Figure 8

1468

1469   Figure 9

1470

1471   Figure 10

1472

1473   Figure 11

1474

1475

1476

1477   Figure 12

1478